

WRDC-TR-89-310

AD-A220 370



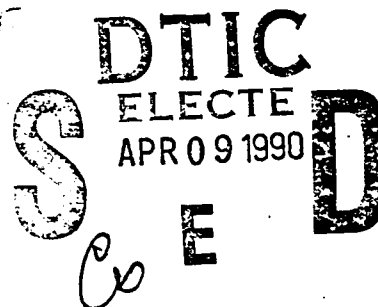
3-D COMPOSITE VELOCITY SOLUTIONS FOR SUBSONIC/TRANSONIC
FLOW OVER FOREBODIES AND AFTERBODIES

Raymond E. Gordnier
Universal Energy Systems
4401 Dayton-Xenia Road
Dayton, Ohio 45432

November 1989

Final Report for Period February 1989 - November 1989

Approved for public release; distribution unlimited




FLIGHT DYNAMICS LABORATORY
WRIGHT RESEARCH DEVELOPMENT CENTER
AIR FORCE SYSTEMS COMMAND
WRIGHT-PATTERSON AIR FORCE BASE, OHIO 45433-6553

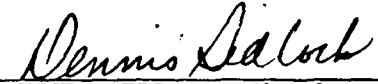
NOTICE

When Government drawing, specifications, or other data are used for any purpose other than in connection with a definitely Government-related procurement, the United States Government incurs no responsibility or any obligation whatsoever. The fact that the government may have formulated or in any way supplied the said drawings, specifications, or other data, is not to be regarded by implication, or otherwise in any manner construed, as licensing the holder, or any other person or corporation; or as conveying any rights or permission to manufacture, use, or sell any patented invention that may in any way be related thereto.


This report is releasable to the National Technical Information Service (NTIS). At NTIS, it will be available to the general public, including foreign nations.

This technical report has been reviewed and is approved for publication.


JOSEPH SHANG
Technical Manager
Computational Aerodynamics


DENNIS SEDLOCK, Chief
Aerodynamics and Airframe Branch
Aeromechanics Division

FOR THE COMMANDER


ALFRED C. DRAPER
Acting Chief
Aeromechanics Division

If your address has changed, if you wish to be removed from our mailing list, or if the addressee is no longer employed by your organization please notify WRDC/FIMM, WPAFB, OH 45433-6553 to help us maintain a current mailing list.

Copies of this report should not be returned unless return is required by security considerations, contractual obligations, or notice on a specific document.

REPORT DOCUMENTATION PAGE				Form Approved OMB No. 0704-0188	
1a REPORT SECURITY CLASSIFICATION Unclassified			1b RESTRICTIVE MARKINGS		
2a SECURITY CLASSIFICATION AUTHORITY			3. DISTRIBUTION/AVAILABILITY OF REPORT Approved for public release; distribution is unlimited.		
2b DECLASSIFICATION/DOWNGRADING SCHEDULE					
4 PERFORMING ORGANIZATION REPORT NUMBER(S)			5. MONITORING ORGANIZATION REPORT NUMBER(S) WRDC-TR-89-3107		
6a NAME OF PERFORMING ORGANIZATION Universal Energy Systems		6b. OFFICE SYMBOL (If applicable) UES	7a. NAME OF MONITORING ORGANIZATION Flight Dynamics Laboratory WRDC/FIMM		
6c ADDRESS (City, State, and ZIP Code) Universal Energy Systems 4401 Dayton-Xenia Road Dayton OH 45433-1894			7b. ADDRESS (City, State, and ZIP Code) Wright-Patterson AFB OH 45433-6553		
8a NAME OF FUNDING/SPONSORING ORGANIZATION Flight Dynamics Laboratory		8b. OFFICE SYMBOL (If applicable) WRDC/FIMM	9 PROCUREMENT INSTRUMENT IDENTIFICATION NUMBER F33615-86-D-3800		
8c. ADDRESS (City, State, and ZIP Code) Wright-Patterson AFB OH 45433-6553			10. SOURCE OF FUNDING NUMBERS		
			PROGRAM ELEMENT NO.	PROJECT NO.	TASK NO.
			61102F	2307	N6
			WORK UNIT ACCESSION NO. 11		
11 TITLE (Include Security Classification) 3-D COMPOSITE VELOCITY SOLUTIONS FOR SUBSONIC/TRANSONIC FLOW OVER FOREBODIES AND AFTERBODIES					
12 PERSONAL AUTHOR(S) Raymond E. Gordnier					
13a. TYPE OF REPORT Final		13b. TIME COVERED FROM 8902 TO 8911		14. DATE OF REPORT (Year, Month, Day) 1989 November	
				15. PAGE COUNT 56	
16 SUPPLEMENTARY NOTATION					
17 COSATI CODES			18. SUBJECT TERMS (Continue on reverse if necessary and identify by block number)		
FIELD	GROUP	SUB-GROUP			
19 ABSTRACT (Continue on reverse if necessary and identify by block number) A composite velocity procedure for the three-dimensional reduced Navier-Stokes equations is developed. In the spirit of matched asymptotic expansions, the velocity components are written as a combined multiplicative and additive composite of viscous like velocities (U,W) and pseudo-potential or inviscid velocities (ϕ_x, ϕ_y, ϕ_z). The solution procedure is then consistent with both asymptotic inviscid flow and boundary layer theory. For Transonic flow cases, the Enquist-Osher flux biasing scheme developed for the full potential equation is used. A quasi-conservation form of the governing equations is used in the shock region to capture the correct rotational behavior. This is combined with the standard nonconservation nonentropy generating form used in nonshock regions. The consistent strongly implicit procedure is coupled with plane relaxation to solve the discretized equations. The composites velocity procedure is applied for the solution of three-dimensional afterbody problems.					
20 DISTRIBUTION/AVAILABILITY OF ABSTRACT <input checked="" type="checkbox"/> UNCLASSIFIED/UNLIMITED <input type="checkbox"/> SAME AS RPT <input type="checkbox"/> DTIC USERS			21. ABSTRACT SECURITY CLASSIFICATION UNCLASSIFIED		
22a NAME OF RESPONSIBLE INDIVIDUAL Joseph J. S. Shang			22b TELEPHONE (Include Area Code) (513) 255-7127		22c OFFICE SYMBOL WRDC/FIMM

Table of Contents

1. Summary.....	1
2. Introduction.....	2
3. The Governing Equations.....	5
4. Boundary Conditions.....	10
5. Numerical Procedure.....	11
5.1 Finite Difference Equations.....	11
5.2 Consistent Coupled Strongly Implicit Procedure.....	15
5.3 Initial Conditions and Convergence Acceleration....	17
5.4 Transonic Flow and Turbulence Model.....	18
6. Results and Discussion.....	20
6.1 Axisymmetric Circular Arc Bump.....	20
6.2 Elliptical Cross Section with Circular Arc Axial Variation.....	22
6.3 Nonaxisymmetric Afterbody Configuration.....	23
7. Future Work.....	26
References.....	28
Nomenclature.....	30

List of Figures

	<u>Page</u>
Figure 1. Simple Three-Dimensional Geometry with a 2:1 Elliptical Cross Section	33
Figure 2. Wall Shear Distribution on an Axisymmetric Circular Arc Bump: $Re=2.03 \times 10^6$, $M_\infty=0.85$	34
Figure 3. Pressure Coefficient on an Axisymmetric Circular Arc Bump: $Re=2.03 \times 10^6$, $M_\infty=0.85$	35
Figure 4. Wall Shear Distribution on an Elliptic Cylinder with a Circular Arc Bump: $Re=2.03 \times 10^6$, $M_\infty=0.9$	36
Figure 5. Pressure Coefficient on an Elliptic Cylinder with a Circular Arc Bump: $Re=2.03 \times 10^6$, $M_\infty=0.9$	37
Figure 6. Nonaxisymmetric Afterbody Geometry	38
Figure 7a. Pressure Coefficient on the Afterbody Configuration: $Re=1.0 \times 10^6$, $M_\infty=0.8$	39
Figure 7b. Wall Shear Distribution on the Afterbody Configuration: $Re=1.0 \times 10^6$, $M_\infty=0.8$	40
Figure 8a. Pressure Coefficient on the Afterbody Configuration: $Re=1.0 \times 10^6$, $M_\infty=0.9$	41
Figure 8b. Wall Shear Distribution on the Afterbody Configuration: $Re=1.0 \times 10^6$, $M_\infty=0.9$	42
Figure 9. Surface Pressure Contours on the Afterbody Configuration: $Re=1.0 \times 10^6$, $M_\infty=0.9$.	43
Figure 10. Pressure Contours in the $X=0.909$ Cross Plane: $Re=1.0 \times 10^6$, $M_\infty=0.9$	44
Figure 11. Pressure Contours in the $X=0.934$ Cross Plane: $Re=1.0 \times 10^6$, $M_\infty=0.9$	45

Acknowledgement

The author wishes to thank Dr. Stanley G. Rubin, University of Cincinnati, for his advice during many useful discussions of this work. The support and encouragement of Dr. Joseph Shang was also greatly appreciated.

1. Summary

The present work developed a three-dimensional composite velocity solution procedure for the reduced Navier-Stokes equations. The scheme developed is consistent with both asymptotic boundary layer and inviscid flow theories. The composite velocity scheme has been differenced to provide second order accurate solutions. Global storage is required for only three variables. If storage becomes a limiting factor, this may be reduced to one variable by coupling the η -momentum and energy equations to the rest of the system. In separated flow regions, we found that only the W_ξ derivatives needed to be upwinded.

To solve the resulting finite difference equations, a standard plane relaxation procedure has been used with a consistent coupled strongly implicit procedure to invert the system at each cross plane. The CCSIP developed is an approximate LU decomposition that provides a solution at each cross plane that is second order accurate with no iterations on the inversion scheme required. This scheme, coupled with a second order accurate quasi-linearization of nonlinear terms provides a global solution procedure that is second order accurate and requires no local iterations at each cross plane.

Results for transonic/turbulent flow over both axisymmetric and nonaxisymmetric geometries have been presented. The composite velocity scheme is an efficient method for solving many three-dimensional problems. Several possible improvements to the algorithm have been pointed out.

2. Introduction

As the field of computational fluid dynamics has matured, the need for solution procedures that can efficiently solve three-dimensional flows with complex viscous/inviscid interactions has become apparent. One technique for solving these problems is to obtain solutions to the time-dependent Navier-Stokes equations using the time asymptotic limit for the steady-state solution. While the rapid advances in computer technology have made this type of solution procedure possible, they are still costly in both computer time and resources.

The reduced Navier-Stokes (RNS) equations provide an attractive alternative to the full time-dependent Navier-Stokes equations for viscous/inviscid interacting flows. This set of equations has been developed to simulate large Reynolds number (Re) asymptotic behavior while retaining a single composite set of equations. The RNS equations are a composite of the full Euler and second-order boundary layer systems. The terms neglected in the Navier-Stokes equations are higher order in Re in an appropriate 'streamline' coordinate system.

The asymptotic nature of the RNS equations may be further exploited by the use of a composite representation for the flow velocities. In the composite velocity formulation, a combination of a multiplicative and additive composite is defined in the spirit of matched asymptotic expansions. Viscous or rotational velocities U and W and a pseudo-potential or inviscid velocity (ϕ_x, ϕ_y, ϕ_z) are specified. The composite velocity formulation is thus consistent with both asymptotic inviscid

flow and boundary layer theory. For inviscid flows, the continuity equation reduces to the full potential equation, and the momentum equations are identically satisfied. In viscous flow regions, the velocities are determined from the continuity equation and the axial and crossflow momentum equations. The normal momentum equation provides a viscous total pressure correction. The composite velocity formulation has been applied previously for the two-dimensional Navier-Stokes equations for both incompressible [1] and compressible flows [2-4]. In previous work by the present author, the composite velocity formulation was applied to the two-dimensional Euler and RNS equations [5-6].

The splitting of the velocities into a composite of viscous and inviscid velocities provides several advantages over primitive variable formulations. Since the full potential equation is the basic equation for the inviscid flow in the composite procedure, the extensive knowledge base for solving this equation for transonic flows may be exploited when developing the solution procedure for the composite velocity system. In particular, techniques for transonic flow developed for the full potential equation may be applied to the composite velocity form of the RNS equations. In the present work, the Enquist-Osher flux biasing procedure [7] is used in supersonic regions. The ability to identify viscous and inviscid velocities allows these terms to be treated numerically appropriate to the asymptotic character of the terms, i.e., marching of the viscous velocities representing the parabolic character of the boundary layer equations and central differencing for the inviscid velocities representing the elliptic nature of inviscid subsonic flow. For separated flows, the two-dimensional composite velocity formulation does not require upwinding in

the separated region, and the three-dimensional formulation requires unwinding for only the azimuthal W_ξ convective derivative.

The composite velocity procedure is applied to the solution of nonaxisymmetric afterbody flows. Solutions to these types of problems can be very important in aft-fuselage-engine integration for fighter aircraft design. The complex viscous/inviscid interactions in these flows provide a computational challenge to any flow solver. The composite velocity procedure provides an efficient alternative to some of the Navier-Stokes procedures currently being used to solve these problems [8-9].

3. The Governing Equations

The governing equations to be solved are given by the three-dimensional, steady, compressible, RNS approximation. These equations have been formulated for a general, nonorthogonal, curvilinear system of coordinates. This allows the use of appropriate 'streamline' coordinate systems and places no restrictions on the type of grid to be used.

The governing equations are now given in their composite velocity formulation. In the spirit of matched asymptotic expansions, the flow velocities are written as

$$u = (U+1)(g^{11}\phi_{\xi} + g^{12}\phi_{\eta} + g^{13}\phi_{\zeta}) = (U+1)u_e \quad (1a)$$

$$v = (g^{21}\phi_{\xi} + g^{22}\phi_{\eta} + g^{23}\phi_{\zeta}) \quad (1b)$$

$$\begin{aligned} w &= (U+1)(g^{31}\phi_{\xi} + g^{32}\phi_{\eta} + g^{33}\phi_{\zeta}) + W \\ &= (U+1)w_e + W \end{aligned} \quad (1c)$$

The composite representations of u and w , the axial and crossflow velocity components, contain two types of terms, irrotational 'pseudo' potential velocities, e.g., ϕ_{ξ} , ϕ_{η} , ϕ_{ζ} and viscous velocities U and W . Since the change in v across the boundary layer is small, the normal velocity is determined solely by the 'pseudo' potential. This particular composite form has the advantage that no additional unknowns are introduced, and the boundary conditions remain easy to implement.

By substituting equations 1(a-c) into the RNS equations, the following system is obtained:

Continuity

$$\frac{\partial}{\partial \xi} (\rho \sqrt{g} (U+1) u_e) + \frac{\partial}{\partial \eta} (\rho \sqrt{g} v) + \frac{\partial}{\partial \zeta} (\rho \sqrt{g} (U+1) w_e) + \frac{\partial}{\partial \zeta} (\rho \sqrt{g} W) = 0 \quad (2)$$

ξ -Momentum Equation

$$\begin{aligned} \frac{1}{\rho \sqrt{g}} \left[\frac{\partial}{\partial \xi} (\rho \sqrt{g} (U^2 + U) u_e^2) + \frac{\partial}{\partial \eta} (\rho \sqrt{g} U v u_e) + \frac{\partial}{\partial \zeta} (\rho \sqrt{g} (U^2 + U) u_e w_e) \right. \\ \left. + \frac{\partial}{\partial \zeta} (\rho \sqrt{g} U W u_e) \right] + U u_e u_{e\xi} + U w_e u_{e\xi} + W u_e u_{e\xi} + \text{curvature terms} = \\ - g^{11} [G_\xi - TS_\xi] - g^{12} [G_\eta - TS_\eta] - g^{13} [G_\zeta - TS_\zeta] + \frac{1}{\rho \sqrt{g}} (\text{viscous terms}) \end{aligned} \quad (3)$$

ζ -Momentum Equation

$$\begin{aligned} \frac{1}{\rho \sqrt{g}} \left[\frac{\partial}{\partial \xi} (\rho \sqrt{g} (U^2 + U) u_e w_e) + \frac{\partial}{\partial \xi} (\rho \sqrt{g} (U+1) W u_e) + \frac{\partial}{\partial \eta} (\rho \sqrt{g} U v w_e) \right. \\ \left. + \frac{\partial}{\partial \eta} (\rho \sqrt{g} v W) + \frac{\partial}{\partial \zeta} (\rho \sqrt{g} (U^2 + U) w_e^2) + \frac{\partial}{\partial \zeta} (\rho \sqrt{g} (2U+1) W w_e) \right. \\ \left. + \frac{\partial}{\partial \zeta} (\rho \sqrt{g} W^2) \right] + U u_e w_{e\xi} + U w_e w_{e\xi} + W w_e w_{e\xi} + \text{curvature terms} = \\ - g^{31} [G_\xi - TS_\xi] - g^{32} [G_\eta - TS_\eta] - g^{33} [G_\zeta - TS_\zeta] + \frac{1}{\rho \sqrt{g}} (\text{viscous terms}) \end{aligned} \quad (4)$$

Normal Momentum Equation

$$\begin{aligned} U u_e v_\xi + (U w_e + W) v_\zeta + \text{curvature terms} = - g^{21} [G_\xi - TS_\xi] \\ - g^{22} [G_\eta - TS_\eta] - g^{23} [G_\zeta - TS_\zeta] \end{aligned} \quad (5)$$

where

$$G = \frac{\gamma}{\gamma-1} \frac{p}{\rho} + \frac{1}{2} g^{ij} u_e^i u_e^j.$$

The energy equation may also be included in the composite velocity system as an equation for temperature. In the present calculations, however, it is replaced with the assumption of constant total enthalpy. This is a valid approximation for the Mach number regime being considered. The new variable, G , that appears in these equations is similar to the total (or Bernoulli-like) pressure. G is not, however, assumed to be constant but is calculated from the solution procedure.

In viscous regions, the composite velocity formulation is representative of the reduced form of the NS equations. The continuity, ξ -momentum, and ζ -momentum equations determine U , W , and ϕ . The temperature, T , is obtained from the energy equation (or total enthalpy H) and the total pressure correction is determined from the η -momentum equation. In the inviscid limit as $U, W \rightarrow 0$, the continuity equation reduces to the full potential equation and the Bernoulli relation, $G = \text{constant}$, is recovered from the momentum equations. Thus equations (3-5) are identically satisfied, and the composite velocity system reduces to the expected representation for an inviscid, irrotational flow.

The composite velocity scheme is formulated to provide full Euler solutions for the outer inviscid flow. If the momentum equations are solved in the present nonconservation form (3-4), however, the full potential solution is recovered for the outer inviscid flow instead; i.e., neither entropy nor vorticity is generated in the outer inviscid flow. This includes flows with captured shock waves. To capture the rotational or Euler shock wave in transonic flows, the ξ -momentum and ζ -momentum equations must be written in a quasi-conservation form [6] as follows:

ξ -Momentum Equation

$$\begin{aligned}
 & \frac{1}{\rho\sqrt{g}} \left[\frac{\partial}{\partial \xi} (\rho\sqrt{g}(U^2+2U)u_e^2) + \frac{\partial}{\partial \eta} (\rho\sqrt{g}Uvu_e) + \frac{\partial}{\partial \xi} (\rho\sqrt{g}(U^2+2U)u_e w_e) \right. \\
 & + \frac{\partial}{\partial \xi} (\rho\sqrt{g}(U+1)Wu_e) \left. \right] + \text{curvature terms} = - \frac{1}{\rho} [g'^1 p_\xi + g'^2 p_\eta + g'^3 p_\zeta] \\
 & - \frac{1}{\rho\sqrt{g}} \left[\frac{\partial}{\partial \xi} (\rho\sqrt{g}u_e^2) + \frac{\partial}{\partial \eta} (\rho\sqrt{g}vu_e) + \frac{\partial}{\partial \xi} (\rho\sqrt{g}u_e w_e) \right] - \text{curvature terms} \\
 & + \frac{1}{\rho\sqrt{g}} (\text{viscous terms})
 \end{aligned} \quad (6)$$

ζ -Momentum Equation

$$\begin{aligned}
 & \frac{1}{\rho\sqrt{g}} \left[\frac{\partial}{\partial \xi} (\rho\sqrt{g}(U^2+2U)u_e w_e) + \frac{\partial}{\partial \xi} (\rho\sqrt{g}(U+1)Wu_e) + \frac{\partial}{\partial \eta} (\rho\sqrt{g}Uvw_e) + \frac{\partial}{\partial \eta} (\rho\sqrt{g}vW) \right. \\
 & + \frac{\partial}{\partial \xi} (\rho\sqrt{g}(U^2+2U)w_e^2) + \frac{\partial}{\partial \xi} (2\rho\sqrt{g}(U+1)Ww_e) + \frac{\partial}{\partial \xi} (\rho\sqrt{g}W^2) \left. \right] \\
 & + \text{curvature terms} = - \frac{1}{\rho} [g'^1 p_\xi + g'^2 p_\eta + g'^3 p_\zeta] \\
 & - \frac{1}{\rho\sqrt{g}} \left[\frac{\partial}{\partial \xi} (\rho\sqrt{g}u_e w_e) + \frac{\partial}{\partial \eta} (\rho\sqrt{g}vw_e) + \frac{\partial}{\partial \xi} (\rho\sqrt{g}w_e^2) \right] - \text{curvature terms} \\
 & + \frac{1}{\rho\sqrt{g}} (\text{viscous terms})
 \end{aligned} \quad (7)$$

The η -momentum equation (5) is retained in nonconservation form and represents the Crocco equation that relates entropy to vorticity.

With the equations in 'conservation' form, the correct entropy rise at the shock wave will now be generated; however, spurious entropy is also generated in nonshock regions. In the present technique, a simple solution to this problem is available. The nonconservative form of the momentum equations (3-5) produces no entropy, but accurately convects

the entropy or vorticity present in the flow. Therefore, this form of the axial momentum equation is used everywhere except in the shock region where equations (6,7) are required. This leads to a solution procedure with the desirable feature of generating the correct entropy rise at the shock wave but not creating spurious entropy in other regions of the flow. The advantage of nonconservative equations away from shock waves and combined conservative/nonconservative systems has been discussed in several studies by other investigators [11].

4. Boundary Conditions

Boundary conditions for the composite velocity formulation may be easily specified. At solid surfaces, the no-slip condition and zero injection conditions are used giving $U=-1$, $W=0$, and $v=0$. The upper boundary is to be sufficiently far from the body that the flowfield is undisturbed. This yields freestream boundary conditions $U=0$, $W=0$, $\phi=\phi_{fs}$, $T=1$, $S=0$. At the outflow, $\xi=\xi_m$, only one boundary condition needs to be applied, $\phi_{\xi\xi}=0$. This, in effect, assumes a weak viscous/inviscid interaction. At the inflow boundary, uniform flow is assumed for all values except at solid boundaries where the no-slip condition is applied. For all geometries presented in this paper, two planes of symmetry exist in the azimuthal direction. In each of these planes, symmetry conditions are applied for U , ϕ , T , S , with antisymmetry conditions for W .

5. Numerical Procedure

The numerical procedure developed for the composite velocity equations is motivated by numerical procedures for potential flows, ϕ , and for boundary layer flows, U , W . In the composite equations, the upstream or acoustic influence is contained wholly in the potential part of the equations, i.e., $\phi_{\xi\xi}$. A standard plane relaxation procedure similar to that for solutions to the full potential equation is used for all ϕ derivatives. The viscous velocities, U and W , are treated as boundary layer velocities and may be marched except in regions of separated flow. The continuity, ξ -momentum, and ζ -momentum equations are solved as a coupled set of equations for U , W , and $\Delta\phi$. The η -momentum equation and energy equation are solved uncoupled from the system for entropy, S , and temperature, T .

5.1 Finite Difference Equations

The composite velocity equations are differenced so that second order accuracy is obtained for all terms. First order accurate differencing for the streamwise derivatives, U_{ξ} and W_{ξ} , is left as an option. The difference form of the continuity, ξ -momentum, and ζ -momentum equations is obtained at (i,j,k) , with central differences at half points. The derivatives of ϕ are then central differenced at the half point locations. This provides the usual three point central difference for $\phi_{\xi\xi}$, $\phi_{\eta\eta}$, and $\phi_{\zeta\zeta}$. In the η - ζ cross plane, the values of U and W at the half-points are determined by averaging the values at

neighboring grid points. In order to provide the proper upwind bias, consistent with the boundary layer marching character of U and W , the values of U and W at $i+1/2$ and $i-1/2$ are represented with upwind approximations as follows:

$$U_{i+1/2} = U_i + \frac{1}{2} \epsilon \sigma_i (U_i - U_{i-1}) \quad (8a)$$

$$U_{i-1/2} = U_{i-1} + \frac{1}{2} \epsilon \sigma_{i-1} (U_{i-1} - U_{i-2}) \quad (8b)$$

where $\epsilon=0$ provides a first order accurate representation and $\epsilon=1$ provides a second order accurate representation.

In separated flows, the representation of $W_{i+1/2}$ and $W_{i-1/2}$ must be modified to provide the proper upwinding for the W_ξ derivative. This is required since W appears as an additive term in the composite representation for w , rather than a term multiplying an inviscid velocity, e.g., U . Therefore the only upstream influence in separated regions comes through upwinding of the W_ξ derivative. The representations for $W_{i+1/2}$ and $W_{i-1/2}$ become

$$W_{i+1/2} = SM^*[W_i + \frac{1}{2} \epsilon \sigma_i (W_i - W_{i-1})] + SP^*[W_{i+1} + \frac{\epsilon}{2\sigma_{i+1}} (W_{i+1} - W_{i+2})] \quad (9a)$$

$$W_{i-1/2} = SM^*[W_{i-1} + \frac{1}{2} \epsilon \sigma_{i-1} (W_{i-1} - W_{i-2})] + SP^*[W_i + \frac{\epsilon}{2\sigma_i} (W_i - W_{i+1})] \quad (9b)$$

where

$$SM = \frac{1}{4} [2 + \text{SGN}(U_{i-1} + 1) + \text{SGN}(U_i + 1)]$$

$$SP = \frac{1}{4} [2 - \text{SGN}(U_{i-1} + 1) - \text{SGN}(U_i + 1)].$$

In equations (9a,b) a backward difference for W_ξ results if $SM=1$ and $SP=0$, and a forward difference results when $SM=0$ and $SP=1$. At separation and reattachment points, $SM=1/2$ and $SP=1/2$, and a central difference is obtained for W_ξ . This provides for a smooth transition between backward and forward differencing at separation and reattachment points.

The first order boundary layer viscous terms are treated implicitly and have been linearized by assuming all inviscid velocities, u_e , v , and w_e known. Since the second order boundary layer terms are small, these terms have been included as an explicit correction, with the inviscid velocities calculated from the previous global iteration and U and W determined from previous marching steps. The combinations $G_\xi - TS_\xi$, $G_\eta - TS_\eta$, and $G_\zeta - TS_\zeta$ also have a minimal influence on the solution of the governing equations. These terms have been uncoupled from the momentum equations and are assumed known from the previous global iteration.

Certain terms must also be lagged so that a stable relaxation procedure is obtained. In the global relaxation process, the only term that introduces ϕ at two different iteration levels is $\phi_{\xi\xi}$. All first derivatives of ϕ in the streamwise direction, ϕ_ξ , and the cross derivatives $\phi_{\xi\eta}$, $\phi_{\xi\zeta}$ are taken from the previous global iteration. All η - ζ cross derivatives are assumed known so that a five point computational star is maintained in the cross plane.

When solving the difference form of the equations, errors arise in the freestream because of incomplete cancellation of metric terms[12].

Essentially, a group of terms that analytically should be zero introduces an error owing to the differencing of metric terms. The following residual term represents the freestream error for the continuity (i.e., full potential) equation

$$FSR = \frac{\partial}{\partial \xi}(\sqrt{g}u_{e_{fs}}) + \frac{\partial}{\partial \eta}(\sqrt{g}v_{fs}) + \frac{\partial}{\partial \zeta}(\sqrt{g}w_{e_{fs}}), \quad (10)$$

where the freestream velocities are calculated from ϕ_{fs} . To exactly reproduce freestream results, this error term is subtracted out of each equation.

The η -momentum equation is solved uncoupled. It is treated as a first order differential equation for entropy, S . The difference form of the equation is centered at $(i-1/2, j+1/2)$ with all terms being central differenced at this location. The terms arising from nonorthogonal grids, $G_{\xi}-TS_{\xi}$ and $G_{\zeta}-TS_{\zeta}$, are taken from the previous global iteration. All other terms in the equation involve U , W , ϕ , which have already been calculated.

Employing the assumptions for the plane relaxation procedure, the final 3×3 system of difference equations to be solved at each cross plane are written as

$$A\Psi_{i,j-1,k}^{n+1} + B\Psi_{i,j,k}^{n+1} + C\Psi_{i,j+1,k}^{n+1} + D\Psi_{i,j,k-1}^{n+1} + E\Psi_{i,j,k+1}^{n+1} = G - F\Psi_{i-1,j,k}^{n+1} - H\Psi_{i+1,j,k}^n \quad (11)$$

where $n+1$ represents the current iteration level; n represents the previous global iteration, and $\Psi = [U, W, \Delta\phi]^T$. Once equation (11) has been

solved, the values of $T_{i-1/2,j,k}$ and $S_{i-1/2,j,k}$ are then updated from the energy and η -momentum equations, respectively.

5.2 Consistent Coupled Strongly Implicit Procedure

To solve the system of difference equations (11) in an efficient and robust manner, a solution algorithm that is noniterative, unconditionally stable, and spatially consistent is required. A noniterative algorithm is important since this algorithm is applied at each cross plane in the marching direction and a number of global iterations is required to obtain a converged solution. An unconditionally stable and spatially consistent scheme is desirable since grid stretching in the marching direction allows for greater flexibility in resolving important flow features with a minimum number of grid points. A limitation on the step size in the marching direction owing to stability restrictions or the need to maintain the spatial consistency of the scheme would make the number of planes required in this direction prohibitive.

A solution algorithm that satisfies the above requirements is the consistent coupled strongly implicit procedure (CCSIP) developed by Khosla and Rubin[13-14]. The consistent CSIP algorithm may be derived from the following recursion relationship:

$$\Psi_{i,j,k} = GM_{j,k} + ET_{j,k}\Psi_{i,j-1,k} + FT_{j,k}\Psi_{j,k+1} \quad (12)$$

where $GM_{j,k}$ is a column matrix and $ET_{j,k}$ and $FT_{j,k}$ are 3×3 matrices. Equation (12) is substituted into equation (11) for $\Psi_{i,j+1,k}$ and

$\Psi_{i,j,k-1}$. The corner points introduced in this substitution are represented as follows:

$$\begin{aligned} \Psi_{i,j+1,k+1}^{n+1} &= \Psi_{i,j+1,k+1}^* - \alpha(\Psi_{i,j+1,k}^* + \Psi_{i,j,k+1}^* - \Psi_{i,j,k}^*) \\ &+ \alpha(\Psi_{i,j+1,k}^{n+1} + \Psi_{i,j,k+1}^{n+1} - \Psi_{i,j,k}^{n+1}) \end{aligned} \quad (13a)$$

$$\begin{aligned} \Psi_{i,j-1,k-1}^{n+1} &= \Psi_{i,j-1,k-1}^* - \alpha(\Psi_{i,j-1,k}^* + \Psi_{i,j,k-1}^* - \Psi_{i,j,k}^*) \\ &+ \alpha(\Psi_{i,j-1,k}^{n+1} + \Psi_{i,j,k-1}^{n+1} - \Psi_{i,j,k}^{n+1}) \end{aligned} \quad (13b)$$

where $\Psi_{i,j,k}^* = [U_{i,j,k}^*, W_{i,j,k}^*, 0]^T$ with U^* and W^* determined from previous marching locations and $0 \leq \alpha \leq 1$. The consistent form of the solution algorithm is obtained when $\alpha=1$. After substitution the terms in equation (11) may be regrouped giving relations for $GM_{j,k}$, $ET_{j,k}$, and $FT_{j,k}$. A simple two pass inversion procedure may now be used to determine the solution in the cross plane.

The CCSIP in its present form, equation (12), is not a symmetric algorithm. This asymmetry in the algorithm can generate asymmetries in the cross plane solution for three-dimensional geometries. These asymmetries in the cross plane solution can lead to a procedure that is globally divergent. Symmetric solutions may be restored by iteration on the corner points (13a,b). A large number of iterations at each cross plane is required to restore the symmetry of the solution, however. An alternative means of obtaining symmetric solutions is to make the CCSIP algorithm symmetric by solving the mirror image of equation (12). The mirror image solution may then be averaged with the solution from equation (12). This averaging produces a symmetric solution in the

cross plane while requiring work corresponding to only one local iteration.

5.3 Initial Conditions and Convergence Acceleration

We have found the present relaxation procedure to be sensitive to the initial guess for ϕ ; the assumption of uniform flow is generally inadequate as an initial condition. Problems associated with the initial conditions may be remedied by starting the viscous solution with the corresponding solution to the inviscid full potential equation. This initial guess may be obtained by solving the inviscid form of the composite velocity equations with slip boundary conditions. An attractive alternative to using the composite system for the potential flow is to use a more efficient code developed strictly for the full potential equation. The composite velocity procedure may then be used to efficiently determine the viscous solution to the problem.

The convergence of the global relaxation procedure for the composite velocity system is determined primarily by the convergence rate for the inviscid flow variable, ϕ . It is well known that plane relaxation procedures slow down dramatically as the number of planes in the marching direction is increased. In the present calculations, solutions are always obtained on the coarsest possible grid; subsequent solutions on finer grids are then initiated with the coarser grid solutions. This allows for more rapid upstream propagation of downstream information.

The previous discussion suggests that convergence could be greatly accelerated using a formal multi-grid procedure. Multi-grid procedures are particularly appealing for the composite velocity system since the

inviscid solution is based on the full potential equation. A uni-directional multi-grid procedure has already been developed by Himansu and Rubin[15] for the RNS equations in primitive variable form. This technique can easily be adapted for the composite velocity system and is recommended for further investigation.

The convergence of the potential flow may also be accelerated by using overrelaxation for the calculation of $\Delta\phi$ in the continuity (i.e., full potential) equation [16]. This introduces a time like term $\phi_{\xi t}$ that provides temporal damping to the system. This additional damping aids in accelerating the convergence of the inviscid flow while introducing no additional error in the converged state.

5.4 Transonic Flow and Turbulence Model

Since the outer inviscid solution of the composite velocity system is based on the full potential equation, techniques for treating the transonic full potential equation may be adopted for the composite velocity system. The flux biasing procedure of Enquist-Osher[7], which specifies a modified density for the full potential equation, is used for the present calculations. This is a simple scheme that has several advantages. The scheme provides monotone profiles through captured shock waves. The captured shocks are very sharp with only a two point transition through the shock wave. The flux biasing scheme also accurately monitors sonic conditions while transitioning through sonic lines. The theoretical reason for these properties lies in the fact that the Enquist-Osher scheme satisfies an "entropy inequality."

The numerical solution of the RNS equations for large Reynolds number flows requires the introduction of a model for turbulence. Algebraic eddy viscosity models provide the simplest means for modelling turbulent flows. Implementation of these models requires minimal computer time and storage. The algebraic eddy viscosity model used in the present work was developed by Baldwin and Lomax[17]. This two-layer model is patterned after the Cebeci-Smith turbulence model, but removes the need for determining the edge of the boundary layer. For the afterbody configurations calculated herein, the Shang and Hankey relaxation model [18] has been used to account for the "memory" of turbulence transport. This is required for flows with large adverse pressure gradients.

6. Results and Discussion

The composite velocity procedure will be used to obtain results for nonaxisymmetric afterbody configurations. To test various aspects of the code, several simpler configurations have also been calculated, *figure 1. A sampling of these results will be presented here. A more extensive discussion of these results is given in references 20 and 21.

6.1 Axisymmetric Circular Arc Bump

The flow over an axisymmetric circular arc bump is used to test the ability of the present technique to calculate turbulent, transonic flows. The particular geometry chosen has been used by Johnson [19] to evaluate the capabilities of various turbulence models to predict inviscid-viscous interactions that occur at transonic conditions. The test model consists of a circular cylinder having a diameter of 15.2 cm with a circular arc bump having a maximum thickness of 1.9 cm and a chord length of 20.3 cm. To eliminate problems from grid discontinuities at the leading and trailing edge of the bump, the sharp corners have been smoothed using a third order polynomial.

In the axial direction, a uniform spacing $\Delta\xi=0.01667$ is specified on the circular arc bump. A uniform stretching factor of $\sigma=1.2$ is specified ahead and aft of the bump with the grid extending 4 chord lengths in each direction and a maximum grid spacing of $\Delta\xi=0.7$. A total

*Figures are located at end of report.

of 105 grid points is used in the axial direction with 61 points on the bump and 22 grid points ahead and aft of the bump. An initial spacing at the wall of $\Delta\eta=0.000025$ is used. A total of 61 grid points is used in the normal direction. The grid spacing at the wall gives a value of $\eta^+ \approx 1$ for the first point away from the wall. The outer boundary is located 6.2 radii from the surface of the cylinder.

Results for a supercritical case, $M_\infty=0.85$ and $Re=2.03 \times 10^6$ based on chord length are given in figures 2 and 3. Comparison of the pressure coefficient with the experimental results of Johnson shows excellent agreement of the shock strength and location. Downstream of the shock, the calculated pressure shows a larger compression than the experimental results in the trailing edge region. From the wall shear results this is a region of reverse flow. The computed separation region lies between $x=0.86$ and $x=1.04$. The experimental results show a separated region of flow between $x=0.815-0.85$ and $x=1.1$. The variance in the separation point in the experimental results arises from the fact that a rapid increase in the size of the separation bubble occurs at $M_\infty=0.85$. The experimental results show a slightly larger separated region than the computed results. The discrepancy in the size of the separated flow region and the pressure results in this region is due to the inability of the turbulence model to adequately treat separated flow regions. The smoothing of the trailing edge may also be causing the computed flow to reattach earlier than the experimental results.

6.2 Elliptical Cross Section with Circular Arc Axial Variation

For the first three-dimensional flow calculations, a cylinder with a 2:1 elliptical cross section is used. A circular arc variation in the axial direction is specified with the major axis having the same axial variation as the previous axisymmetric geometry. A grid size of $109 \times 61 \times 17$ is used to calculate the present results. A uniform spacing of $\Delta\xi = 0.01667$ is specified on the bump with a grid stretching factor of 1.2 specified ahead and aft of the bump. The grid is stretched to a maximum grid spacing of $\Delta\xi = 0.125$ which is then held constant. The grid extends 2.27 chord lengths ahead and aft of the body. In the azimuthal direction, a uniform spacing $\Delta\zeta = 0.098$ radians is specified. The normal grid distribution is the same as that used for the axisymmetric calculations.

The flow calculated is for $Re = 2.03 \times 10^6$ and $M_\infty = 0.9$. A turbulent boundary layer profile is specified at the inflow. The axial variation of the wall shear and the pressure coefficient for several azimuthal locations is given in figures 4 and 5. The wall shear shows a substantial variation in the azimuthal direction while the pressure coefficient shows less variation except near the leading and trailing edge. There is a sharp decrease in wall shear around $x = 0.3$ and then a plateau region before the decrease in wall shear owing to the shock. This behavior is due to the curvature effects of the geometry on the boundary layer near this symmetry plane. The shock strength and location show very little variation in the azimuthal direction.

The effects of grid resolution in both the axial and azimuthal direction were also investigated for this geometric configuration. The predominant effect of grid refinement is on the wall shear distribution in the region of the shock. Grid refinement has a minimal effect on the pressure coefficient. The effect of second order accuracy for the U_ξ and W_ξ derivatives has also been investigated with the main effect again being on the wall shear distribution in the region of the shock. A more detailed discussion of these results is again found in references [20-21].

6.3 Nonaxisymmetric Afterbody Configuration

The nonaxisymmetric afterbody configuration for which calculations are to be made is shown in figure 6. The geometry consists of a main body section with an elliptical cross section of aspect ratio 1.097. The upper symmetry plane transitions to a final boattail angle of 17.6° , while the side symmetry plane transitions to a final boattail angle of 6.7° . A solid sting is used to simulate the nozzle exhaust plume. The final aspect ratio of the elliptical cross section is 1.94. A third order polynomial is used to smooth the discontinuity at the juncture of the boattail with the sting.

The flow fields calculated are doubly symmetric and only one quarter of the flow field is calculated. A grid of $146 \times 65 \times 17$ grid points is used. Twenty-eight planes are used to resolve the boattail with the spacing on the boattail being 0.4% of the total body length. Sixty-five grid points are used in the body normal direction with a minimum spacing

at the wall of 0.001% of the body length and the outer boundary located approximately one body length away.

The first case calculated for this geometry is for $M_\infty = 0.8$ and $Re = 1.0 \times 10^6$. The flow remains completely subsonic for this freestream Mach number. The pressure coefficient and wall shear distribution for various $\eta = \text{const}$ lines are given in figures 7a,b. The beginning of the boattail is located at $x=0.88$. Large azimuthal variations in the pressure and wall shear on the boattail are seen. At the point of minimum pressure, there is a 20% variation in pressure from the top to side symmetry plane. The point of minimum pressure on the side symmetry plane occurs slightly forward of the minimum pressure location on the top symmetry plane.

The methods for accelerating the calculations described earlier were used for these results. A total of 1 hour, 25 minutes, and 22 seconds of CPU time on the Cray XMP were required for this calculation. Of the total time, 52 minutes and 11 seconds or 61% of the time is spent calculating the potential flow used as an initial condition for the viscous calculation. This time can be greatly reduced by using a code designed specifically for calculating potential flows. Thus with a potential flow solution to the problem, a viscous flow solution may be obtained in only 33 minutes and 11 seconds. The amount of memory required for this calculation is 907,776 words.

The pressure coefficient and wall shear distribution for a transonic case, $M_\infty = 0.9$, are given in figures 8a,b. A large azimuthal variation in both the pressure and the wall shear distribution can again be seen. The shock wave on the top symmetry plane is much stronger and is located

further aft on the boattail. A 24% variation in the minimum pressure is seen. A small region of reverse flow induced by the shock wave/boundary layer interaction can be seen in the wall shear distribution just downstream of the shock wave.

Plots of pressure and Mach contours show a clearer picture of the flowfield characteristics. Figure 9 gives surface pressure contours in the boattail region. The expansion region terminating in a shock wave can clearly be seen. This region has a greater axial extent along the top symmetry plane, and the shock wave again appears much stronger. Pressure contours in two cross planes located at $x=0.909$ and $x=0.934$ are given in figures 10 and 11 respectively. These again show the three-dimensional effects in the flowfield. In particular, there is a very large azimuthal variation in the pressure in the $x=0.934$ cross plane, which is located in the shock region.

Mach contours in the top and side symmetry planes are given in figures 12 and 13 respectively which clearly show the sharp shock waves generated by the Enquist-Osher flux biasing procedure. The shock is again much stronger on the top symmetry plane. The effect of the shock on the boundary layer can also be seen with the boundary layer becoming thinner in the region ahead of the shock and thickening as the boundary layer interacts with the shock wave.

Figures 14 and 15 show the effect of viscosity on the pressure coefficient along the top and side symmetry planes. The viscous effects tend to weaken and diffuse the shock with the viscous shock being located slightly upstream of the potential shock. The viscous flow also undergoes a much smaller compression in the boattail juncture region.

6. Future Work

We have noted several possible needed improvements to the current composite velocity scheme during the course of these calculations. An improved downstream boundary condition that more accurately represents the three-dimensional effects at this boundary is required. We have found the solution procedure to be sensitive to the downstream boundary condition in a very local region near this boundary. The current implementation of the $v=0$ boundary condition on the body also needs to be improved so that $v=0$ is maintained for each global iteration. This should improve the convergence performance of the algorithm. Finally, work is currently under way to replace the CCSIP algorithm with a direct sparse matrix solver. This should further improve the robustness of the present numerical scheme.

References

1. Rubin, S. G. and Khosla, P. K., "A Composite Velocity Procedure for the Incompressible Navier-Stokes Equations," 8th International Conference on Numerical Methods in Fluid Mechanics, Springer-Verlag, 1982, pp.448-454.
2. Khosla, P. K. and Rubin S. G., "A Composite Velocity for the Compressible Navier-Stokes Equations," AIAA Journal, Vol. 21, No. 11, November, 1983, pp. 1546-1551.
3. Swanson, R. C., Rubin, S. G. and Khosla, P. K., "Calculations of Afterbody Flows with a Composite Velocity Formulation," AIAA Paper No. 83-1736, July, 1983.
4. Rubin, S. G., Celestina, M. and Khosla, P. K., "Second-Order Composite Velocity Solutions for Large Reynolds Number Flows," AIAA Paper No. 84-0172, January, 1984.
5. Gordnier, R. E., "Transonic Viscous and Inviscid Solutions Using a Composite Velocity Procedure," AIAA Paper No. 86-0074, January, 1986.
6. Gordnier, R. E. and Rubin, S. G., "Transonic Flow Solutions Using a Composite Velocity Procedure for Potential, Euler, and RNS Equations," Computers and Fluids, 17, 1, pp 85-98, 1989.
7. Osher, S., Hafez, M. and Whitlow, "Entropy Condition Satisfying Approximations for the Full Potential Equation of Transonic Flow," Mathematics of Computation, Vol. 44, No. 169, January, 1985, pp. 1-29.

8. Wilmoth, R. G. and Putnam, L. E., "Subsonic/Transonic Prediction Capabilities for Nozzle/Afterbody Configurations," AIAA Paper No. 84-0192, January, 1984.
9. Compton, W. B., Thomas, J. L., Abeyounis, W. K., and Mason, M. L., "Transonic Navier-Stokes Solutions of Three-Dimensional Afterbody Flows and Comparison with Experiment," proposed NASA TP.
10. Rizzi, A., "Spurious Entropy Production and Very Accurate Solutions to the Euler Equations," AIAA Paper No. 84-1644, June, 1984.
11. Pandolfi, M. "The Merging of Two Different Ideas: A Shock Fitting Performed by a Shock Capturing," International Symposium On Computational Fluid Dynamics, Tokyo, September, 1985.
12. Shankar, V., Ide, H., Gorski, J., and Osher, S., "A Fast Time Accurate Unsteady Full Potential Scheme," AIAA Paper No. 85-1512, July, 1985.
13. Khosla, P. K. and Rubin, S. G., "Consistent Strongly Implicit Iterative Procedures," Proceedings of the 10th International Conference on Numerical Methods in Fluid Dynamics, Springer-Verlag, June, 1986.
14. Khosla, P. K. and Rubin, S. G., "Consistent Strongly Implicit Iterative Procedures for Two-Dimensional Unsteady and Three-Dimensional Space-Marching Flow Calculations," Computers and Fluids, Vol. 15 No. 4, 1987, pp. 361-377.
15. Himansu, A. and Rubin, S. G., "Multigrid Acceleration of a Relaxation Procedure for the RNS Equations," AIAA Paper No. 87-1145-CP, June, 1987.

16. Bradley, P. F., Dwyer, D. L., South, J.C, and Keen, J. M.,
"Vectorized Schemes for Conical Potential Flow Using the Artificial
Density Method," AIAA Journal, Vol. 24, No. 1, January, 1986.
17. Baldwin, B. S. and Lomax, H., "Thin Layer Approximations and
Algebraic Model for Separated Turbulent Flows," AIAA Paper No.
78-257, January, 1978.
18. Shang, J. S. and Hankey, W. L., "Numerical Solutions for Supersonic
Turbulent Flow Over a Compression Ramp," AIAA Journal, Vol. 13,
No. 10, October, 1975, pp. 1368-1374.
19. Johnson, D. A., "Transonic Separated Flow Predictions with an Eddy
Viscosity/Reynolds Stress Closure Model," AIAA Journal, Vol. 25,
No. 2, February, 1987, pp. 252-259.
20. Gordnier, R. E., "A Composite Velocity Procedure for the Three-
Dimensional Reduced Navier-Stokes Equations," Ph.D. Dissertation,
Department of Aerospace Engineering and Engineering Mechanics,
University of Cincinnati, 1988.
21. Gordnier, R. E. and Rubin, S. G., "3-D Composite Velocity Solutions
for Subsonic/Transonic Flows," Proceedings of the Fourth Symposium
on Numerical and Physical Aspects of Aerodynamic Flows, January,
1989.

Nomenclature

C_f	skin friction coefficient
C_p	pressure coefficient
c_p	specific heat at constant pressure
F_{kleb}	Klebanoff intermittency factor
g_{ij}, g^{ij}	metric tensors
g	determinant of the metric tensor $ g_{ij} $
G	Bernoulli pressure term
H	total enthalpy
M	Mach number
p	pressure
q	speed
Re	Reynolds number
S	entropy
SM, SP	switches for forward and backward differencing
T	temperature
u	velocity component in axial direction
U	viscous composite velocity component in axial direction
u_e	inviscid velocity in axial direction
v	velocity component in body normal direction
w	velocity component in azimuthal direction
W	viscous composite velocity component in azimuthal direction

w_e	inviscid velocity in azimuthal direction
x, y, z	Cartesian coordinates
β, σ_m	factors for stretched grid in normal direction
γ	ratio of specific heats
Γ_{ij}^k	Christoffel symbol of the second kind
ϵ	switch for first or second order accuracy
ξ, η, ζ	coordinates in computational plane
η^+	$\frac{\sqrt{\rho_w \omega _w} \eta}{\mu_w}$, law of the wall coordinate
θ	azimuthal location - $\sqrt{y^2 + z^2}$
μ, λ	coefficients of viscosity
μ_t	eddy viscosity
ρ	density
σ	grid stretching factor
ϕ	potential like function
$\Delta\phi$	$\phi^{n+1} - \phi^n$
Ψ	$[U, W, \Delta\phi]^T$
ω	vorticity

Subscripts

t, x, y, z	derivatives
ξ, η, ζ	
i, j, k	indexes for coordinate directions or counters for tensor notation
\cdot, j	covariant derivative
∞, fs	freestream
m	maximum
w	wall value

Superscripts

i, j, k	counters for tensor notation
$n+1$	new iteration level
n	old iteration level

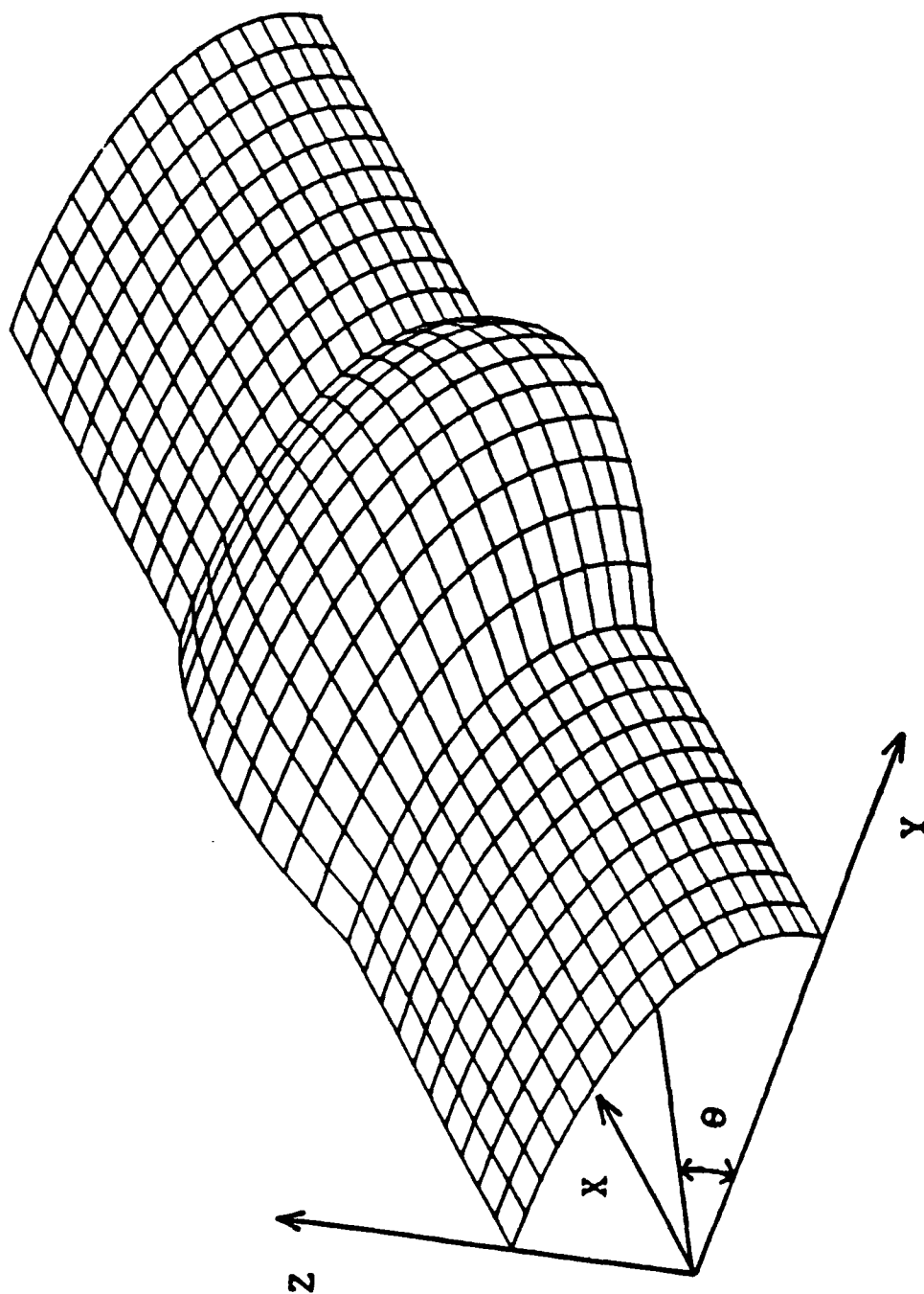


Figure 1. Simple Three-Dimensional Geometry with a 2:1 Elliptical Cross Section

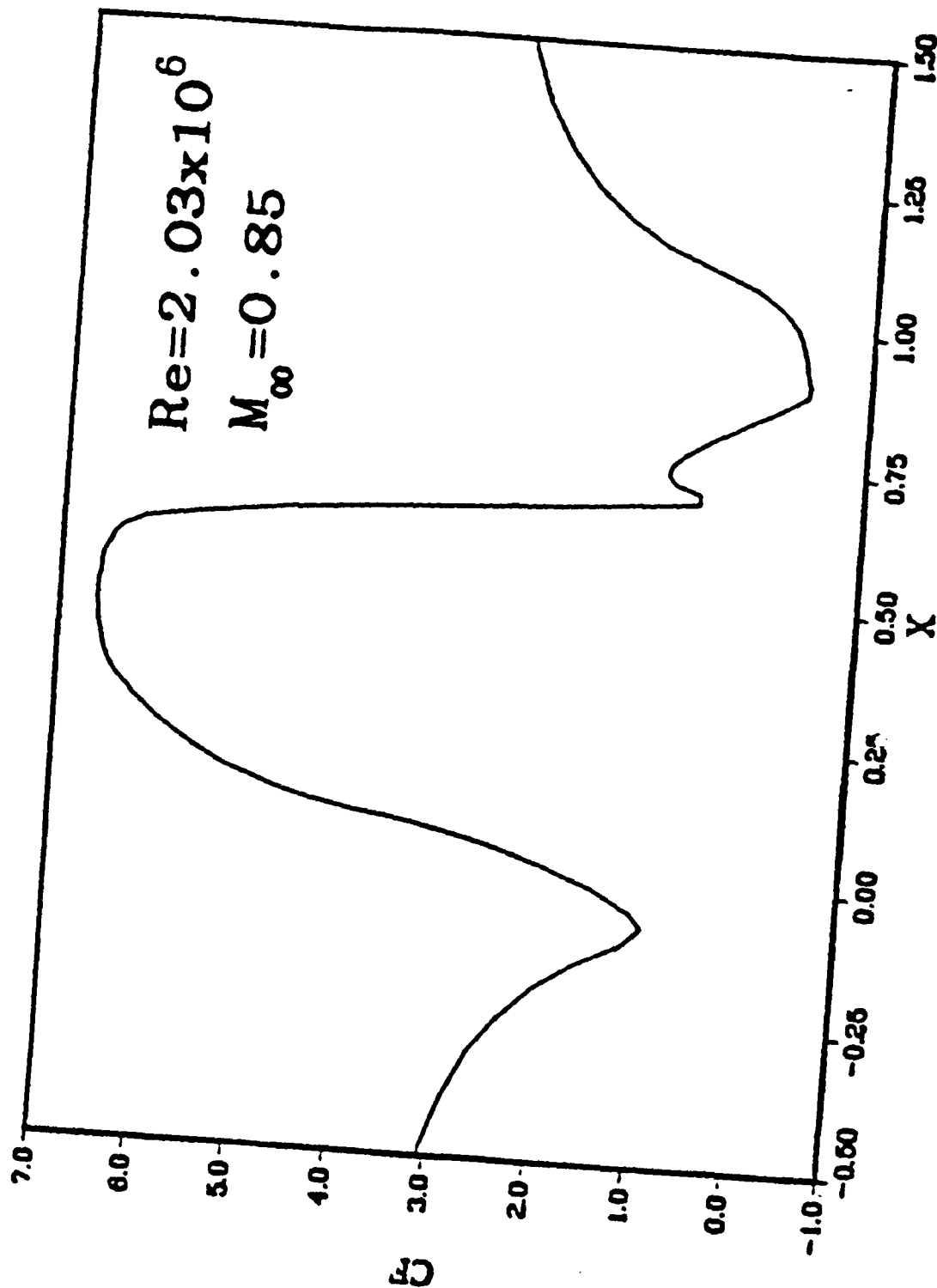


Figure 2. Wall Shear Distribution on an Axisymmetric Circular Arc Bump:
 $Re = 2.03 \times 10^6$, $M_{\infty} = 0.85$

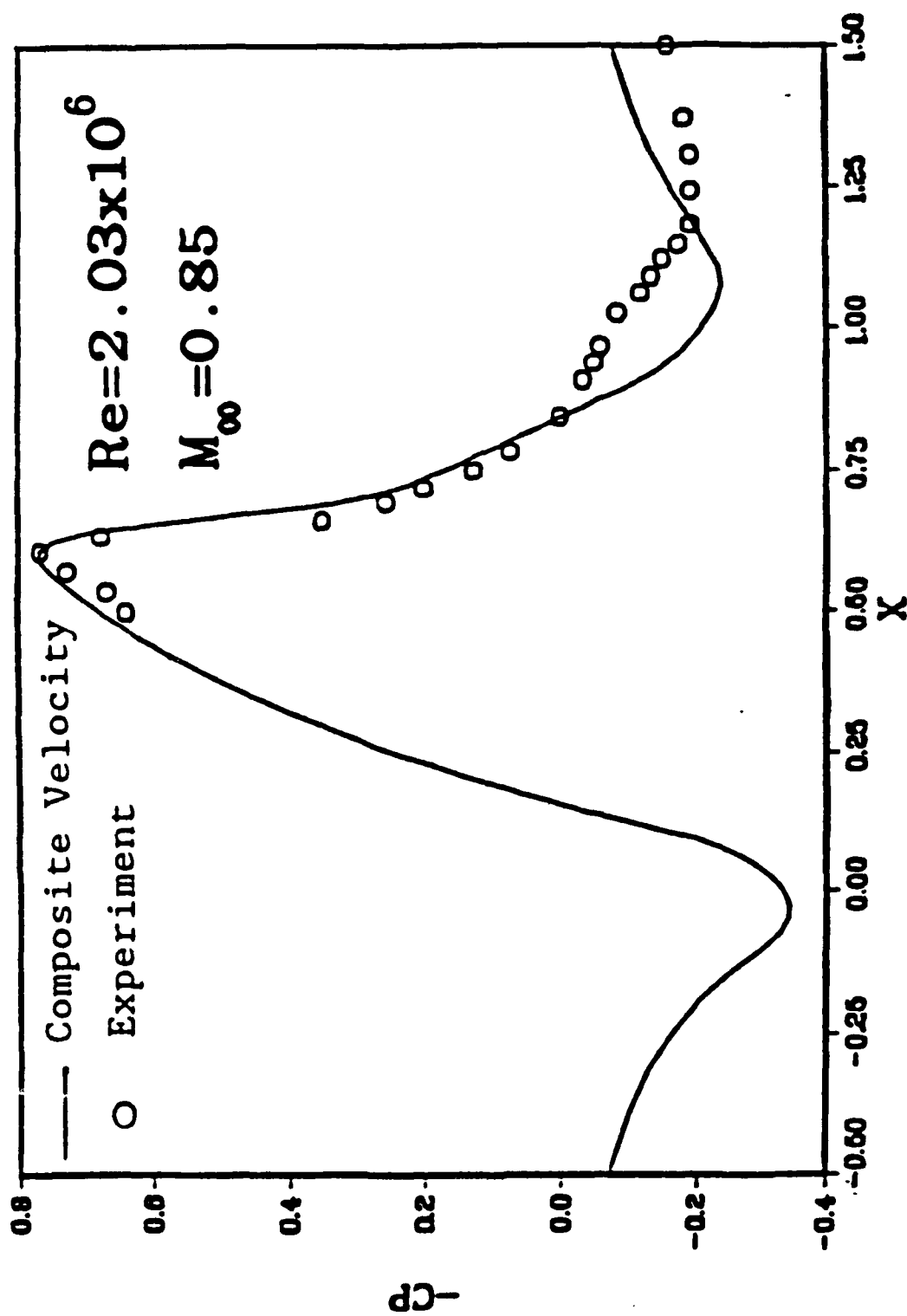


Figure 3. Pressure Coefficient on an Axisymmetric Circular Arc Bump:
 $Re = 2.03 \times 10^6$, $M_\infty = 0.85$

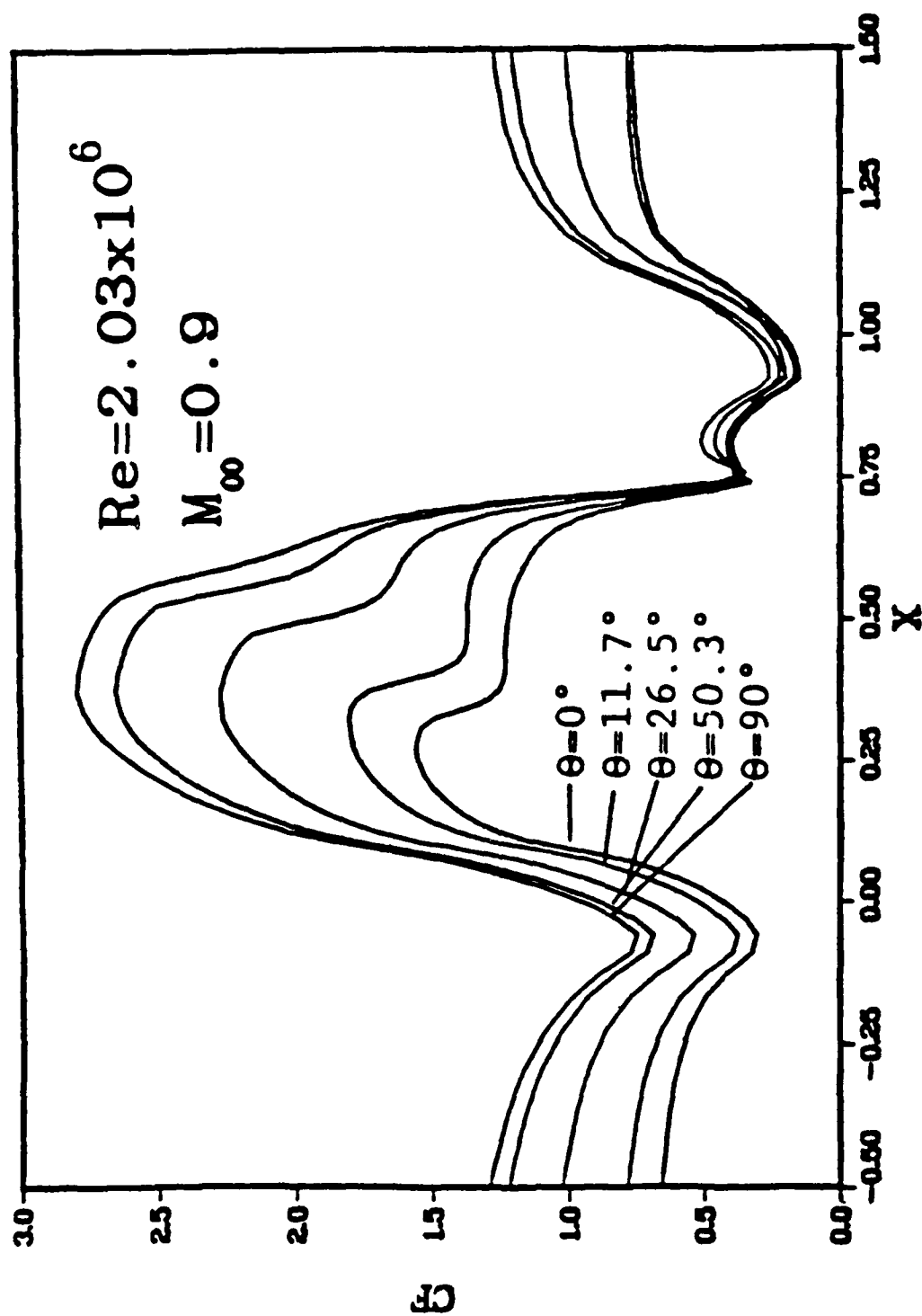


Figure 4. Wall Shear Distribution on an Elliptic Cylinder with a Circular Arc Bump: $Re=2.03 \times 10^6$, $M_\infty=0.9$

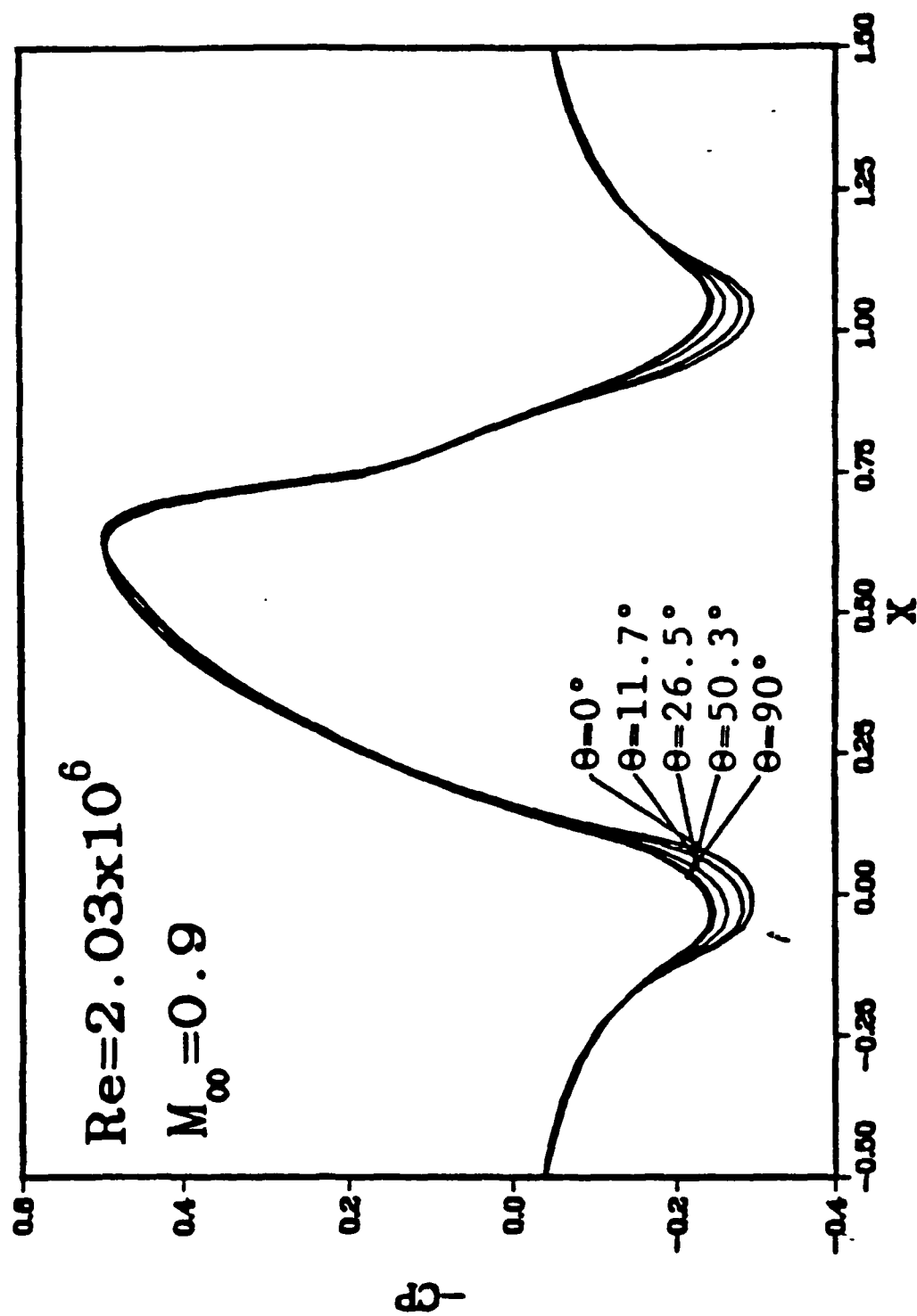


Figure 5. Pressure Coefficient on an Elliptic Cylinder with a Circular Arc Bump: $Re = 2.03 \times 10^6$, $M_\infty = 0.9$

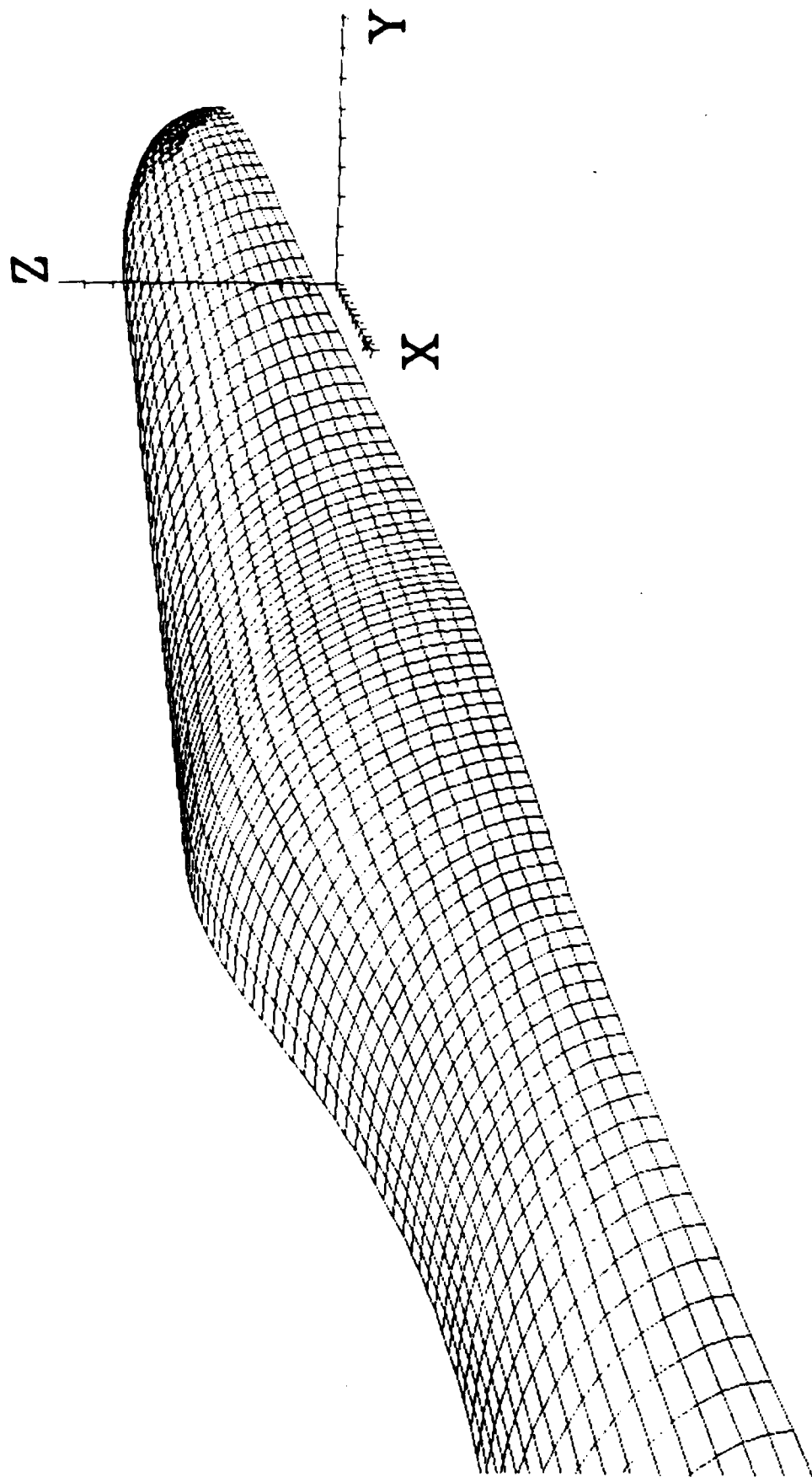


Figure 6. Nonaxisymmetric Afterbody Geometry

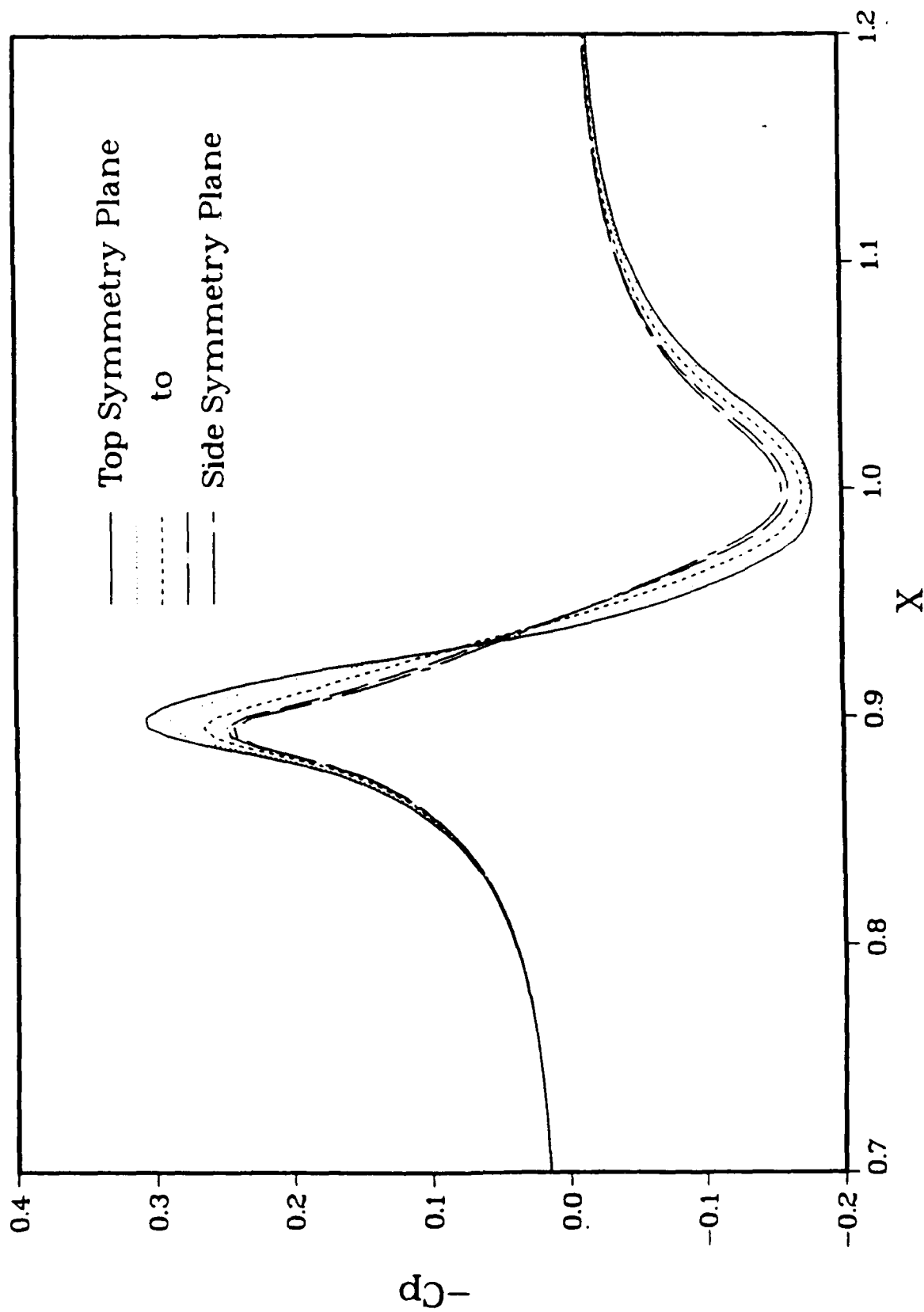


Figure 7a. Pressure Coefficient on the Afterbody Configuration:
 $Re=1.0 \times 10^6$, $M_\infty = 0.8$

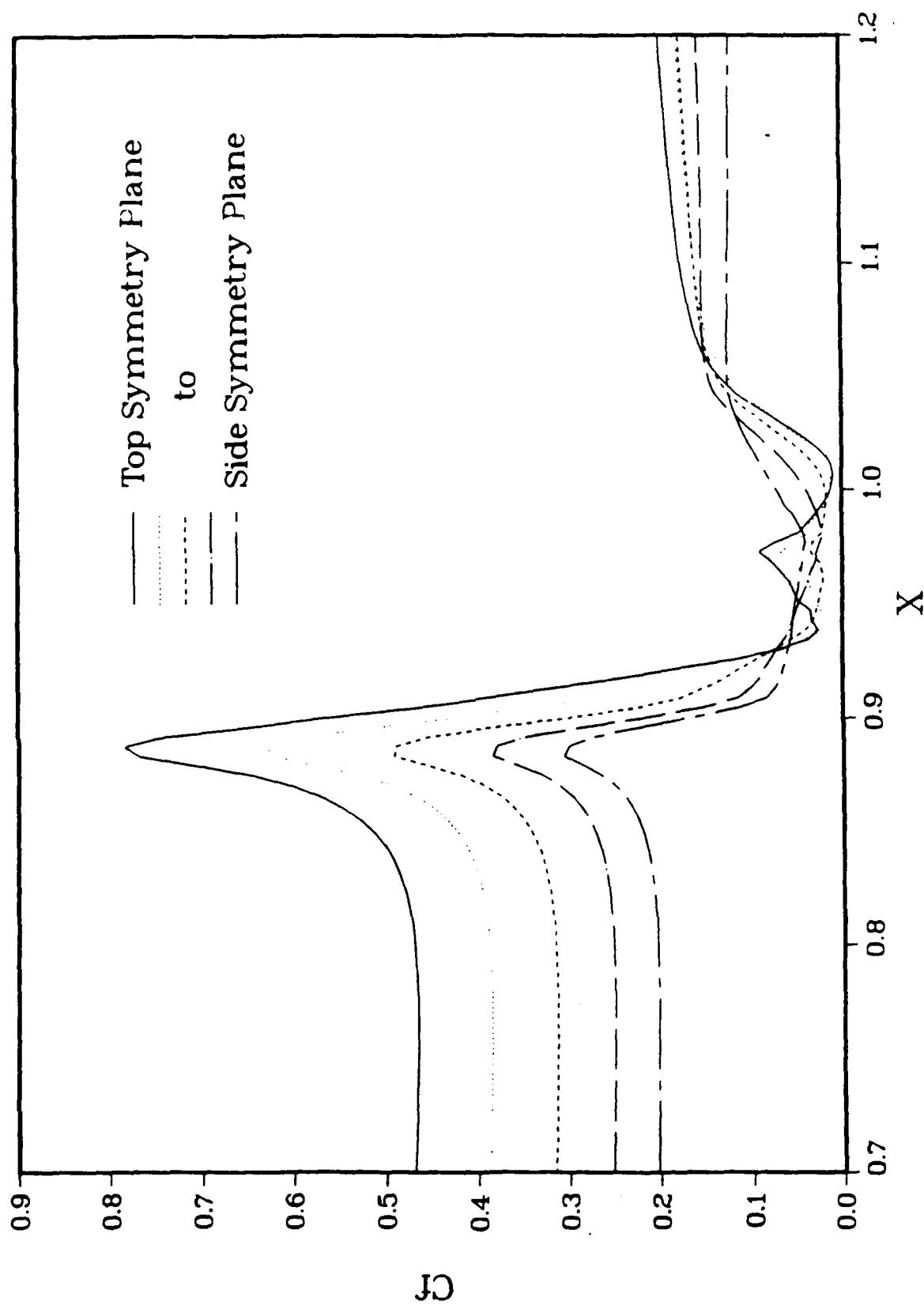


Figure 7b. Wall Shear Distribution on the Afterbody Configuration:

$Re = 1.0 \times 10^6$, $M_\infty = 0.8$

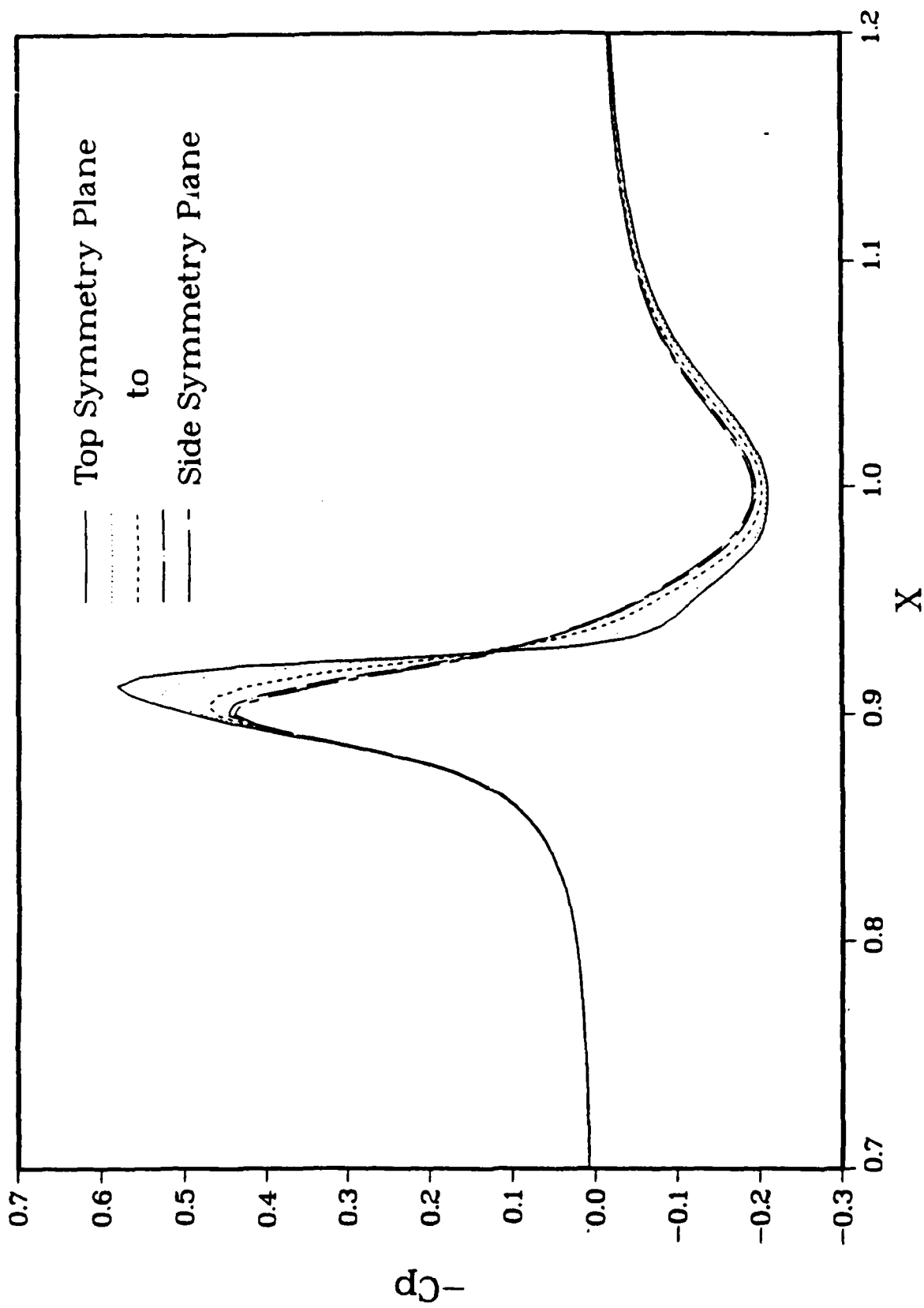


Figure 8a. Pressure Coefficient on the Afterbody Configuration:

$Re=1.0 \times 10^6$, $M_\infty = 0.9$

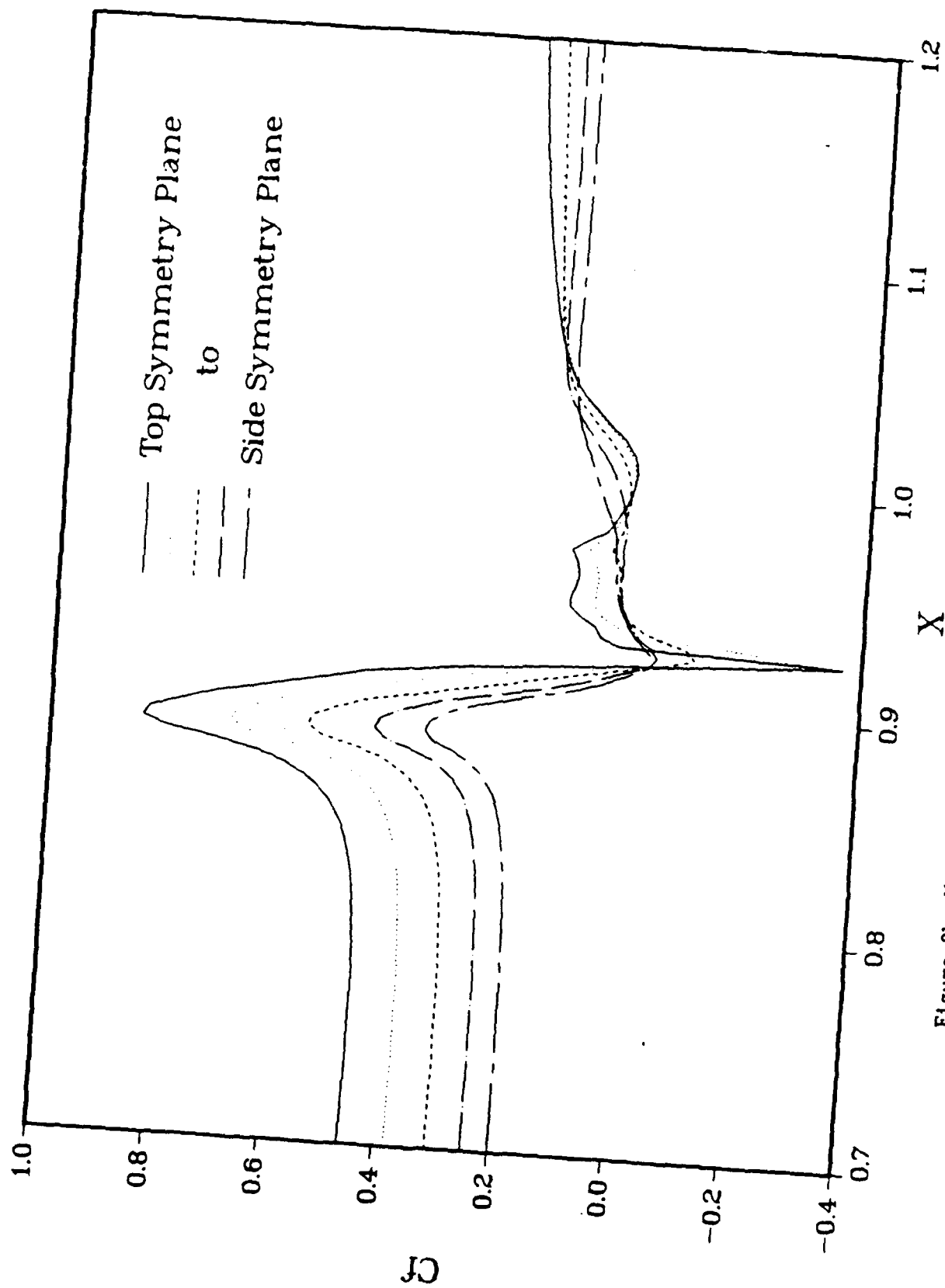


Figure 8b. Wall Shear Distribution on the Afterbody Configuration:
 $Re=1.0 \times 10^6$, $M_\infty = 0.9$

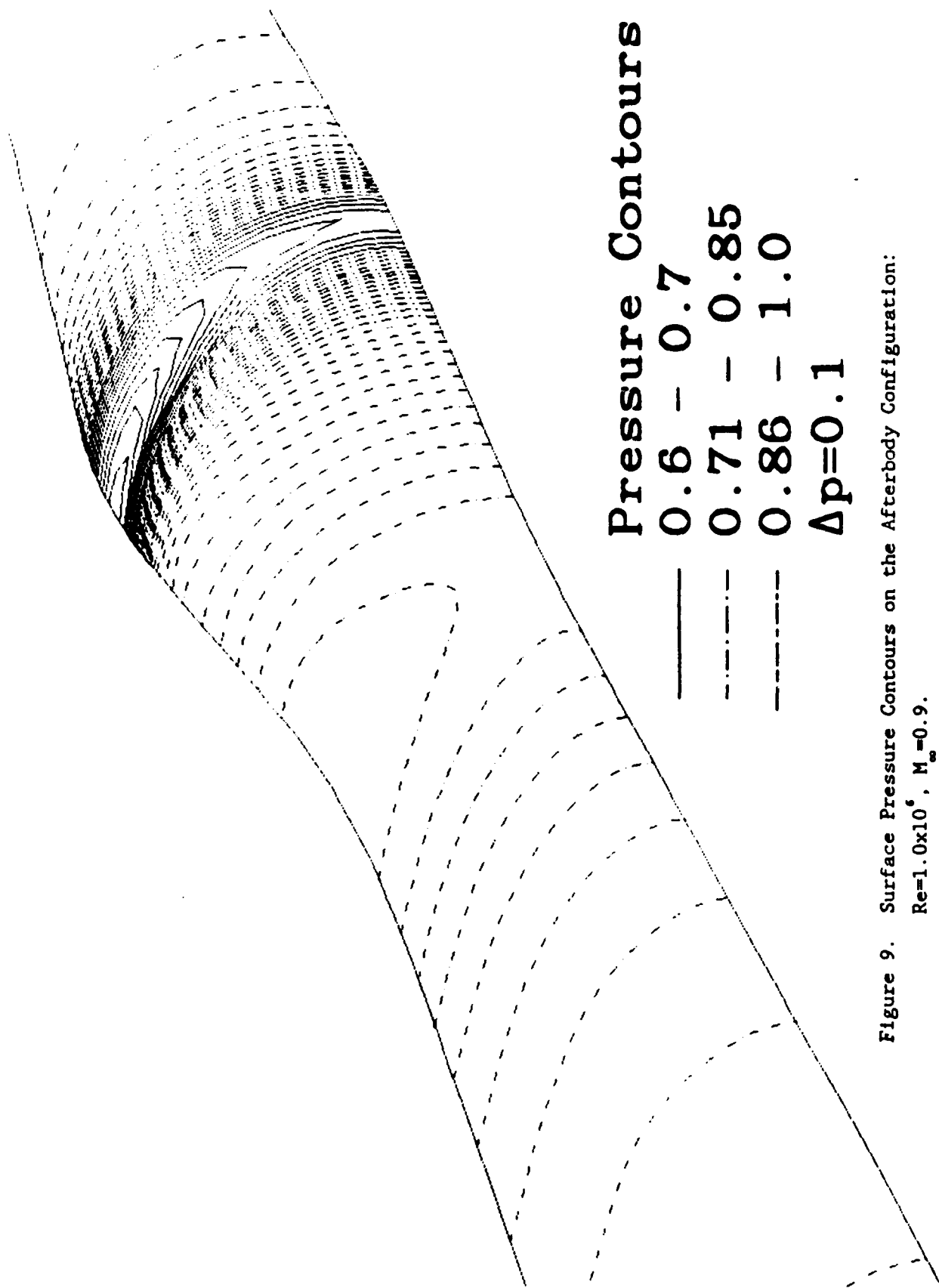


Figure 9. Surface Pressure Contours on the Afterbody Configuration:
 $Re=1.0 \times 10^6$, $M_\infty=0.9$.

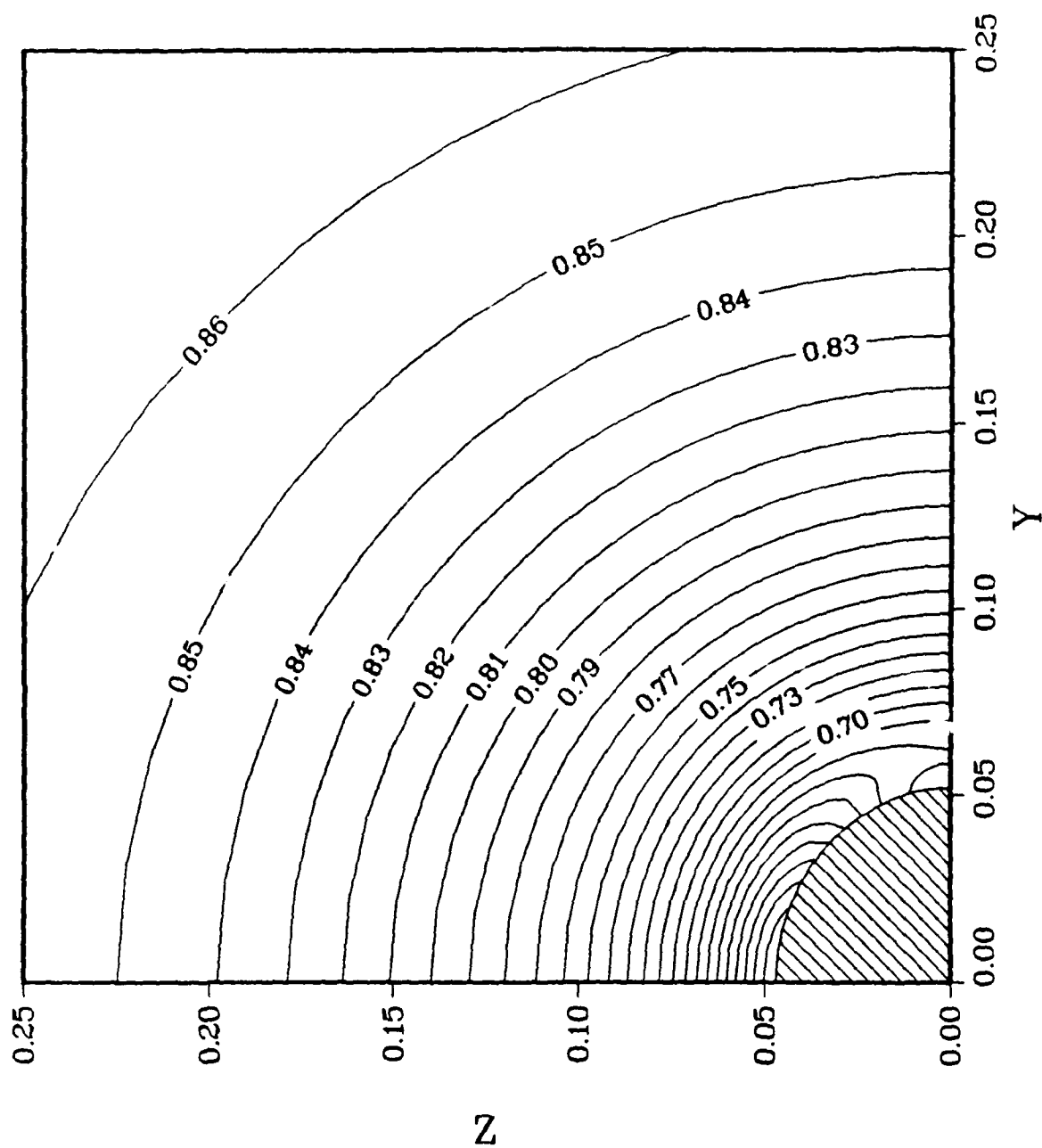


Figure 10. Pressure Contours in the $X=0.909$ Cross Plane: $Re=1.0 \times 10^6$,
 $M_\infty = 0.9$

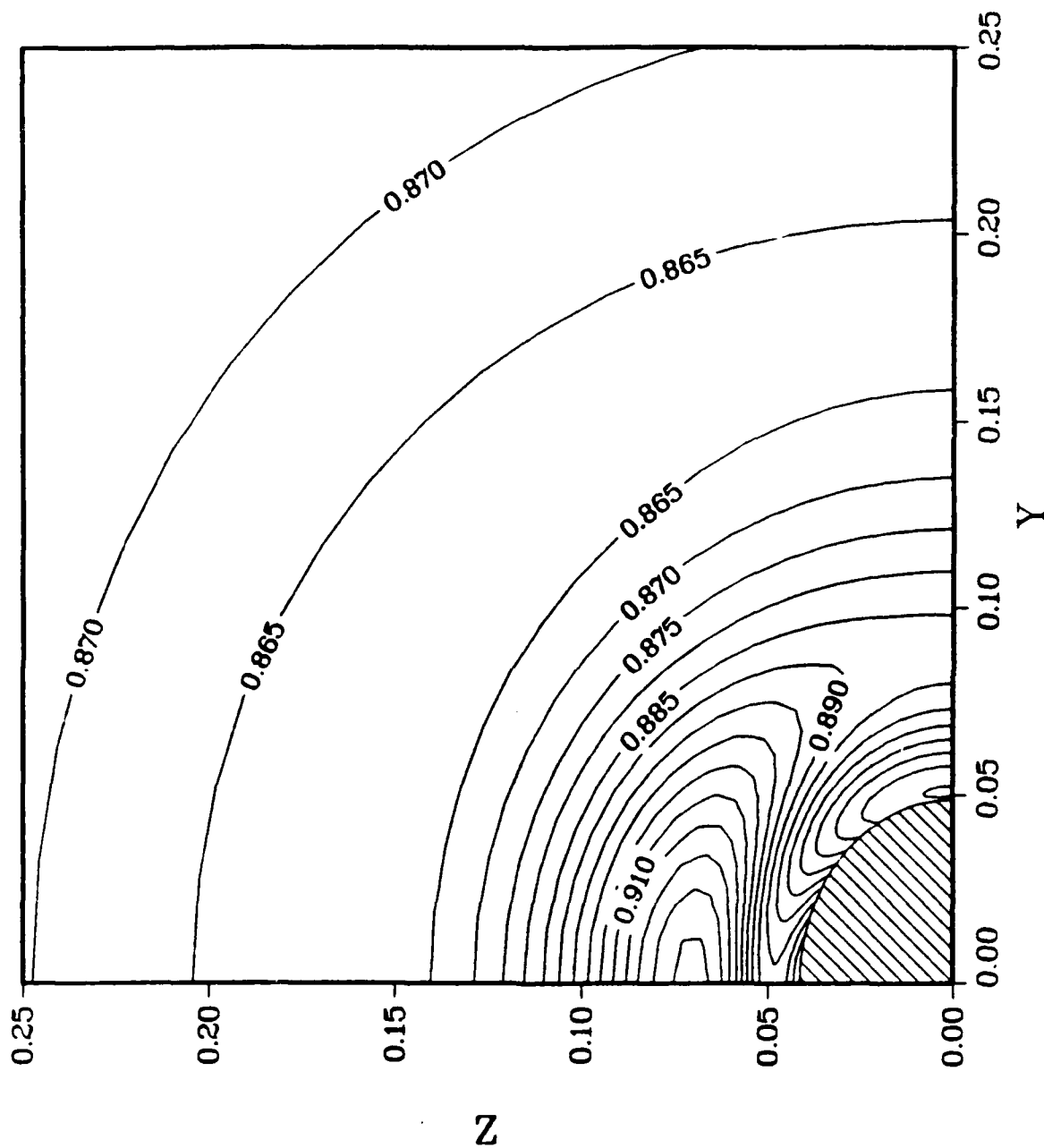


Figure 11. Pressure Contours in the $X=0.934$ Cross Plane: $Re=1.0 \times 10^6$, $M_\infty=0.9$

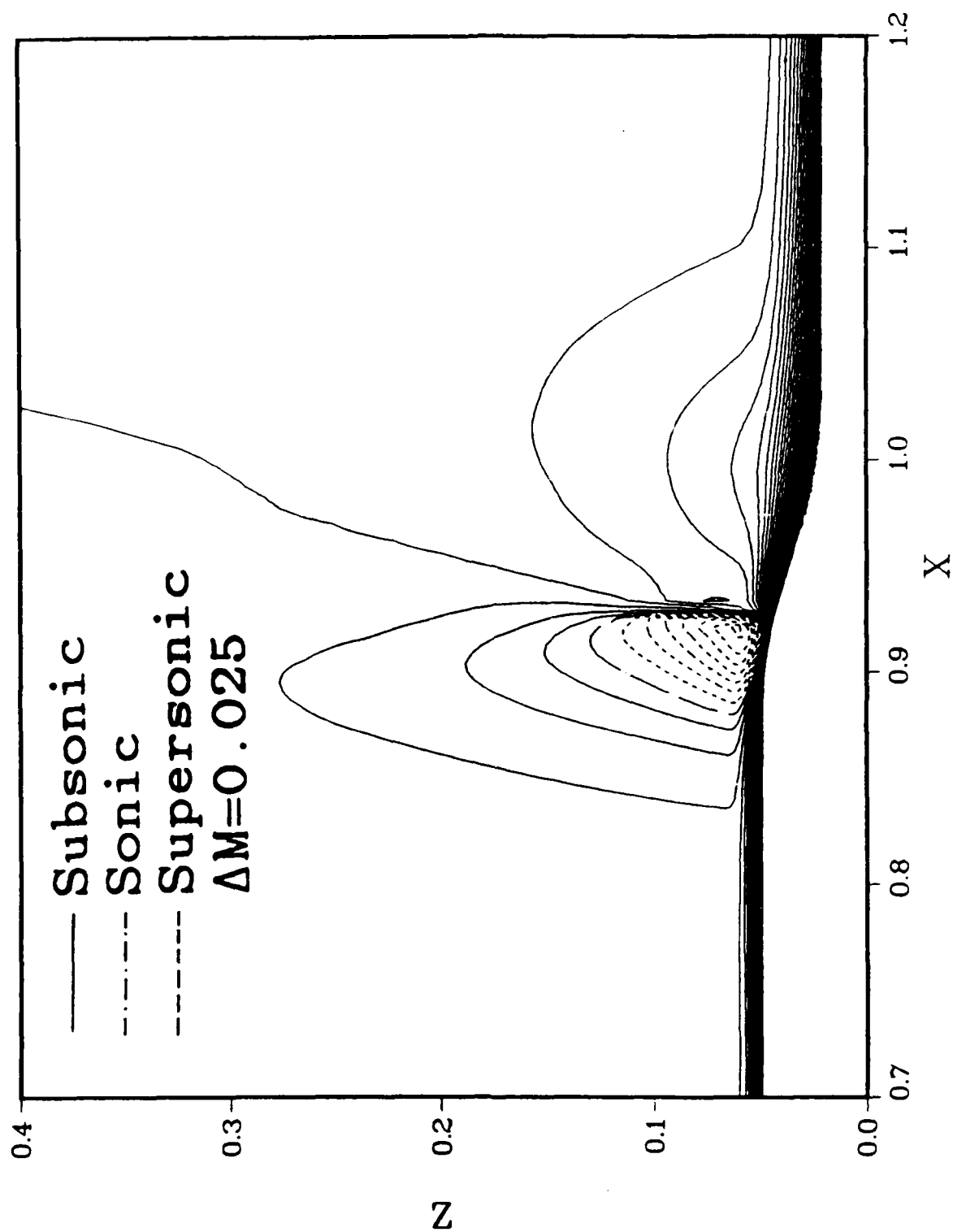


Figure 12. Mach Contours in the Top Symmetry Plane: $Re = 1.0 \times 10^6$, $M_\infty = 0.9$

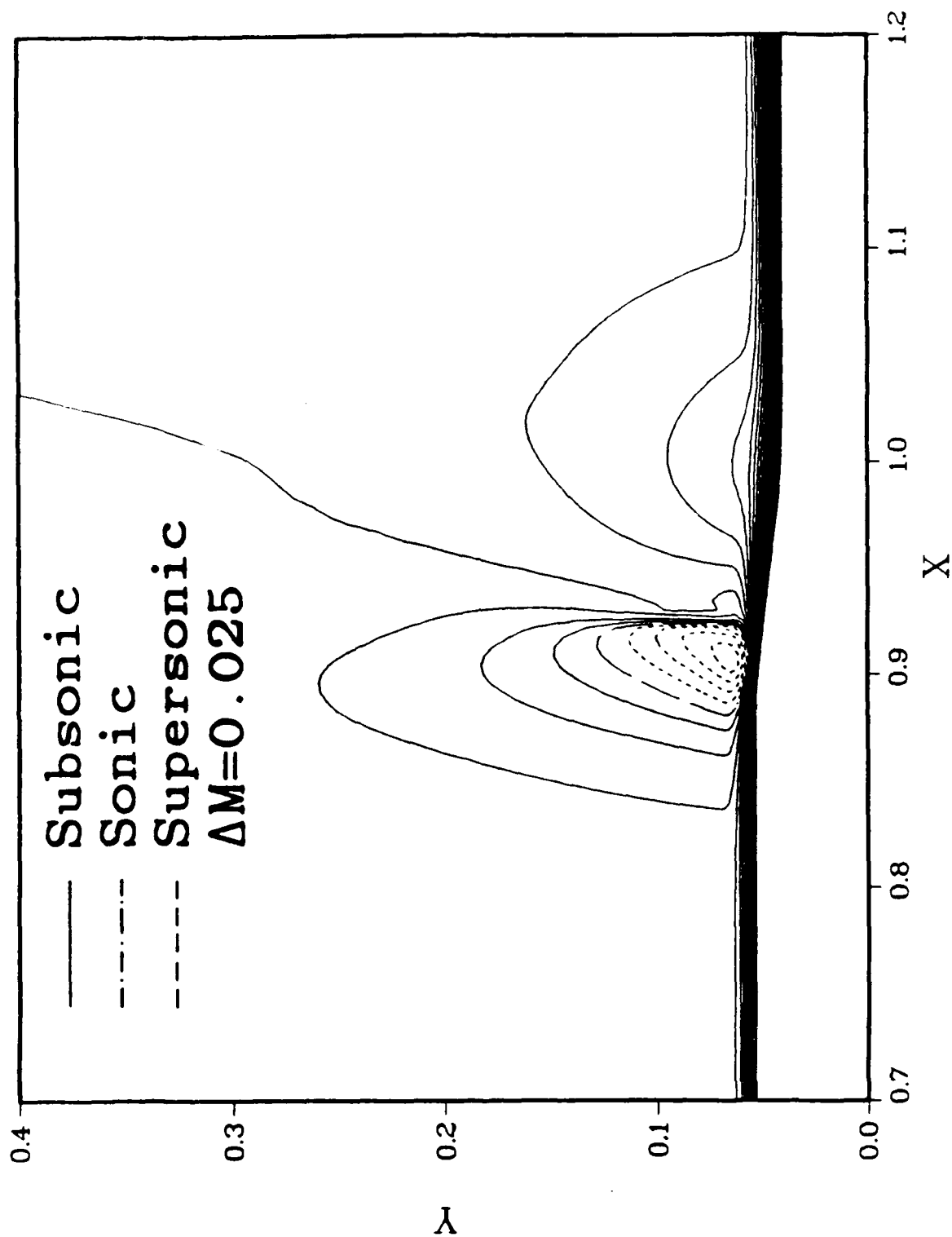


Figure 13. Mach Contours in the Side Symmetry Plane: $Re = 1.0 \times 10^6$, $M_\infty = 0.9$

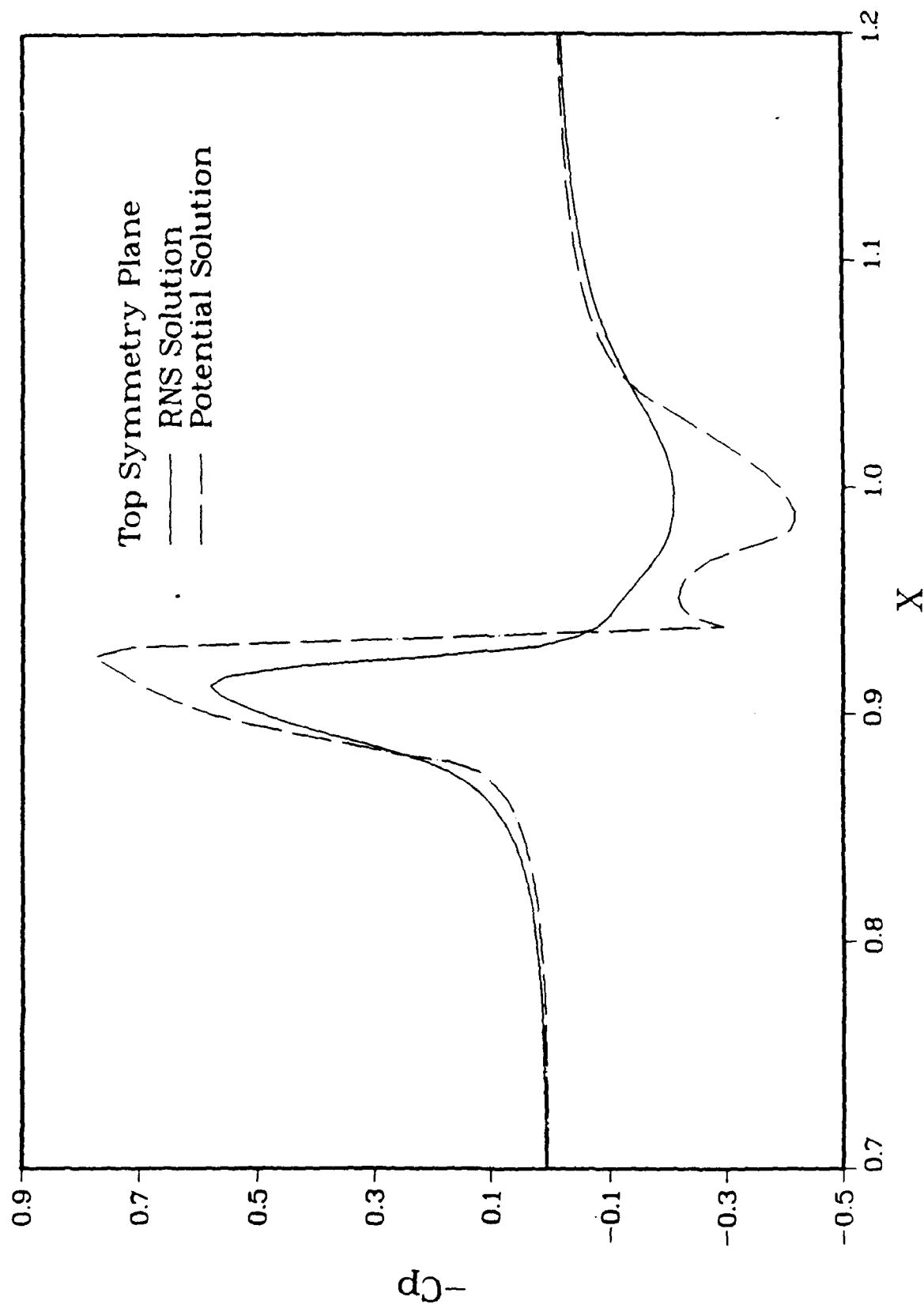


Figure 14. Effect of Viscosity on the Surface Pressure Coefficient:
 $Re=1.0 \times 10^6$, $M_\infty = 0.9$

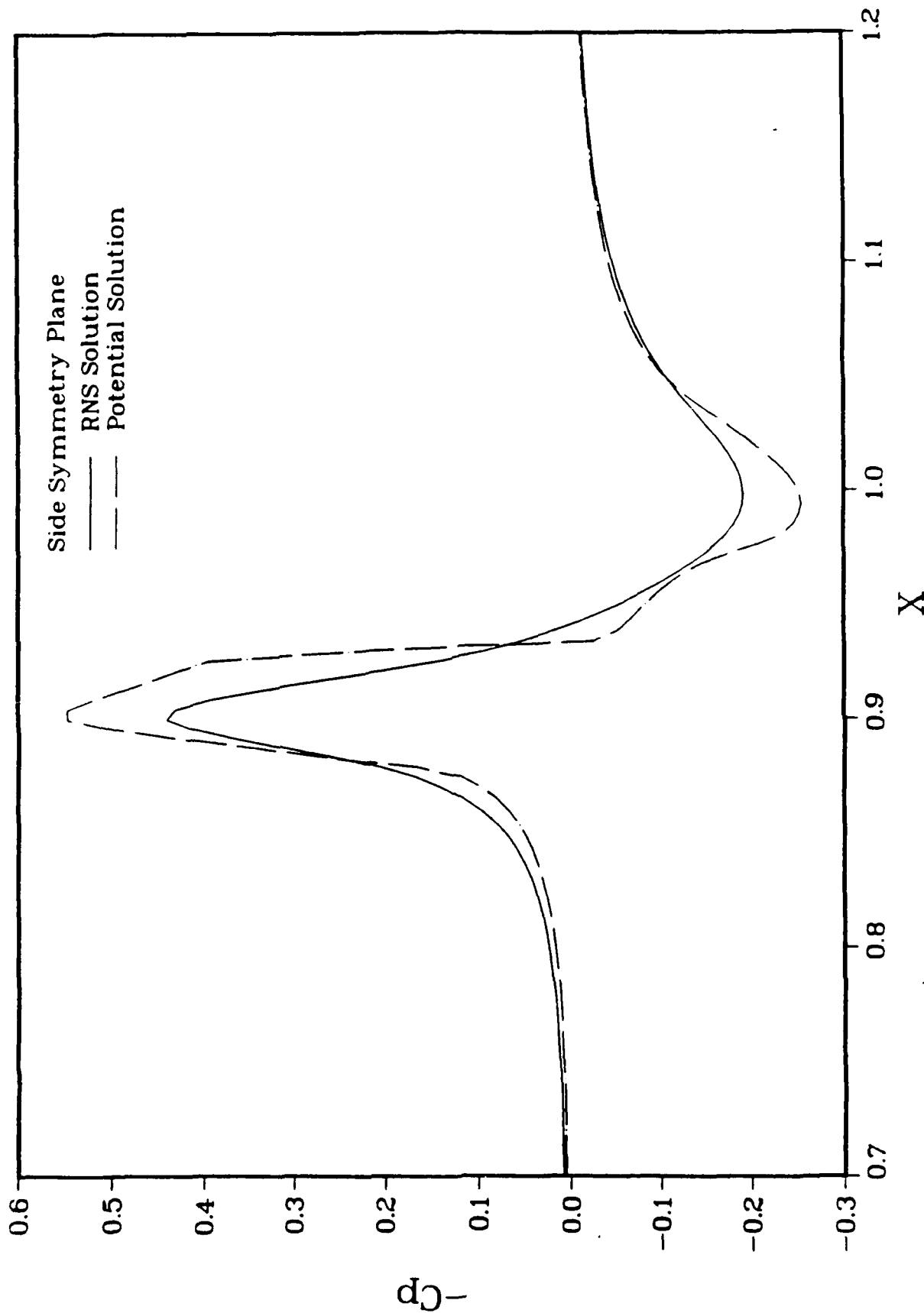


Figure 15. Effect of Viscosity on the Surface Pressure Coefficient:
 $Re=1.0 \times 10^6$, $M_\infty=0.9$